Pontifícia Universidade Católica
do Rio de Janeiro

Stélio Henrique Lopes Neto

Three-dimensional flow of thixotropic liquids in coating dies

Dissertação de Mestrado

Dissertation presented to the Programa de Pós–graduação em Engenharia Mecânica, do Departamento de Engenharia Mecânica da PUC-Rio in partial fulfillment of the requirements for the degree of Mestre em Engenharia Mecânica.

Advisor : Prof. Márcio da Silveira Carvalho
Co-advisor: Dr. Sergio Santiago Ribeiro
Co-advisor: Prof. Florian Alain Yannick Pradelle

Rio de Janeiro
February 2025

Pontifícia Universidade Católica
do Rio de Janeiro

Stélio Henrique Lopes Neto

Three-dimensional flow of thixotropic liquids in coating dies

Dissertation presented to the Programa de Pós–graduação em Engenharia Mecânica da PUC-Rio in partial fulfillment of the requirements for the degree of Mestre em Engenharia Mecânica. Approved by the Examination Committee:

Prof. Márcio da Silveira Carvalho
Advisor
Departamento de Engenharia Mecânica – PUC-Rio

Dr. Sergio Santiago Ribeiro
Co-advisor
Departamento de Engenharia Mecânica – PUC-Rio

Prof. Florian Alain Yannick Pradelle
Co-advisor
Departamento de Engenharia Mecânica – PUC-Rio

Prof. Paulo Roberto de Souza Mendes
Departamento de Engenharia Mecânica – PUC-Rio

Prof. Jaewook Nam
School of Chemical and Biological Engineering – SNU, South Korea

Rio de Janeiro, February 18th, 2025

Stélio Henrique Lopes Neto

Stélio Henrique Lopes graduated in Mechanical Engineering at Pontifical Catholic University of Rio de Janeiro(PUC-Rio) in 2022.

Bibliographic data

Lopes Neto, Stélio Henrique

Three-dimensional flow of thixotropic liquids in coating dies / Stélio Henrique Lopes Neto; advisor: Márcio da Silveira Carvalho; co-advisores: Sergio Santiago Ribeiro, Florian Alain Yannick Pradelle. – 2025.

74 f: il. color. ; 30 cm

Dissertação (mestrado) - Pontifícia Universidade Católica do Rio de Janeiro, Departamento de Engenharia Mecânica, 2025.

Inclui bibliografia

1. Engenharia Mecânica – Teses. 2. Tixotropia. 3. Processos de Revestimento. 4. Elementos Finitos em 3D. I. Carvalho, Márcio da Silveira. II. Ribeiro, Sergio Santiago. III. Pradelle, Florian Alain Yannick. IV. Pontifícia Universidade Católica do Rio de Janeiro. Departamento de Engenharia Mecânica. V. Título.

CDD: 621

To my parents and family, for always supporting me.

Acknowledgments

To my family, especially my parents, for their constant support and encouragement throughout this journey.

To my love, Mariah, for your patience, your support, and for pretending to be interested when I talked about mesh refinement and non-Newtonian fluids.

To my advisor, Prof. Márcio Carvalho, for his trust, guidance and support throughout this research.

to my co-advisor, Dr. Sergio Ribeiro, for his support and contributions to this work.

To my colleagues in the LMMP group, for the stimulating discussions and shared experiences.

To CAPES, FAPERJ and PUC-Rio, for finantial support.

This study was financed in part by the Coordenação de Aperfeiçoamento de Pessoal de Nível Superior- Brasil (CAPES)- Finance Code 001.

Abstract

Lopes Neto, Stélio Henrique; Carvalho, Márcio da Silveira (Advisor); Ribeiro, Sergio Santiago (Co-Advisor); Pradelle, Florian Alain Yannick (Co-Advisor). **Three-dimensional flow of thixotropic liquids in coating dies**. Rio de Janeiro, 2025. 74p. Dissertação de Mestrado – Departamento de Engenharia Mecânica, Pontifícia Universidade Católica do Rio de Janeiro.

Slot coating is largely used in the manufacturing of different functional films, including battery electrodes. For optimum performance, the thickness of the film deposited over the moving substrate must be uniform along the cross-web direction. The flow uniformity is achieved by properly designing the geometry of the internal cavities of the coating die. The optimized design is strongly influenced by the liquid rheology, which needs to be accurately described in the flow models. The rheological behavior of particle suspensions, as those encountered in slot coating of battery electrodes, is very complex. The viscosity varies orders of magnitude with the shear rate, and they show thixotropic behavior. Usually, flow models used in the design of slot die cavities do not take into account the time dependency of particle suspensions and the flow is described assuming that the local viscosity is only a function of the local deformation rate. This can lead to inaccurate description of the flow, since the liquid structure does not change instantaneously after a step change to a new stress level. This study addresses the three-dimensional internal flow of thixotropic fluids. Time-dependent behavior is modeled using a kinetic equation for the material fluidity, which is defined as the reciprocal of viscosity, and specifies uniquely the material microscopic state. The model accounts for the mechanisms of buildup and breakdown of the microstructure with no postulated functions nor additional auxiliary parameters. A 3D finite element numerical model, implemented in *Python*, based on the precompiled library named *Dolfin*, developed within the open-source project *FeniCs*, allows for a realistic representation of thixotropic fluid flow in complex geometries, such as those present in the internal cavities of slot coating dies. The results show the effect of thixotropy in the flow behavior and how they should be included in the design of slot dies used for coating particle suspensions.

Keywords

Thixotropy; Coating Processes; 3D Finite Element Modeling.

Resumo

Lopes Neto, Stélio Henrique; Carvalho, Márcio da Silveira; Ribeiro, Sergio Santiago; Pradelle, Florian Alain Yannick. **Escoamento tridimensional de fluidos tixotrópicos em barras de revestimento**. Rio de Janeiro, 2025. 74p. Dissertação de Mestrado – Departamento de Engenharia Mecânica, Pontifícia Universidade Católica do Rio de Janeiro.

A técnica de revestimento por fenda é amplamente utilizada na fabricação de diversos filmes funcionais, incluindo eletrodos de baterias. Para um desempenho ideal, a espessura do filme depositado sobre o substrato em movimento deve ser uniforme ao longo da direção transversal. A uniformidade do fluxo é alcançada por meio de um projeto adequado da geometria das cavidades internas da barra de revestimento. O projeto otimizado é fortemente influenciado pela reologia do líquido, que precisa ser descrita com precisão nos modelos de escoamento. O comportamento reológico de suspensões de partículas, como as encontradas no revestimento de eletrodos de baterias, é muito complexo. A viscosidade varia em ordens de magnitude com a taxa de cisalhamento, e essas suspensões exibem comportamento tixotrópico. Geralmente, os modelos de escoamento utilizados no projeto das cavidades da barra de revestimento não consideram a dependência temporal da viscosidade das suspensões de partículas, e o escoamento é descrito assumindo que a viscosidade local é apenas uma função da taxa de deformação local. Isso pode levar a uma descrição imprecisa do escoamento, uma vez que a estrutura do líquido não muda instantaneamente após uma mudança abrupta para um novo nível de tensão. Este estudo aborda o escoamento interno tridimensional de fluidos tixotrópicos. O comportamento dependente do tempo é modelado usando uma equação cinética para a fluidez do material, que é definida como o inverso da viscosidade e especifica exclusivamente o estado microscópico do material. O modelo leva em consideração os mecanismos de construção e desagregação da microestrutura, sem funções postuladas nem parâmetros auxiliares adicionais. Um modelo numérico de elementos finitos tridimensional, implementado em *Python* e baseado na biblioteca pré-compilada chamada *Dolfin*, desenvolvida dentro do projeto de código aberto *FeniCs*, permite uma representação realista do escoamento de fluidos tixotrópicos em geometrias complexas, como as presentes nas cavidades internas das barras de revestimento por fenda. Os resultados mostram o efeito da tixotropia no comportamento do escoamento e

como ela deve ser incluída no projeto de barras de revestimento usadas para revestir suspensões de partículas.

Palavras-chave

Tixotropia; Processos de Revestimento; Elementos Finitos em 3D.

Table of contents

List of figures

List of tables

"What we know is a drop, what we don't know is an ocean."

Isaac Newton.

1
Introduction

1.1
Coating process

Coating is a fundamental process in modern fabrication techniques. In this process, one or more liquid layers are deposited on a solid surface, often a moving flexible substrate. The wet thickness of the coated films varies with the product, typically on the order of 1 to 100 microns, or more. These layers are then dried or cured to form solid films that serve specific functions (KISTLER; SCHWEIZER, 1997).

Figure 1.1 depicts a schematic representation of a coating line. It outlines the basic steps of applying a thin layer of liquid (coating) onto a continuously moving substrate, such as a rolled paper or metal sheet.

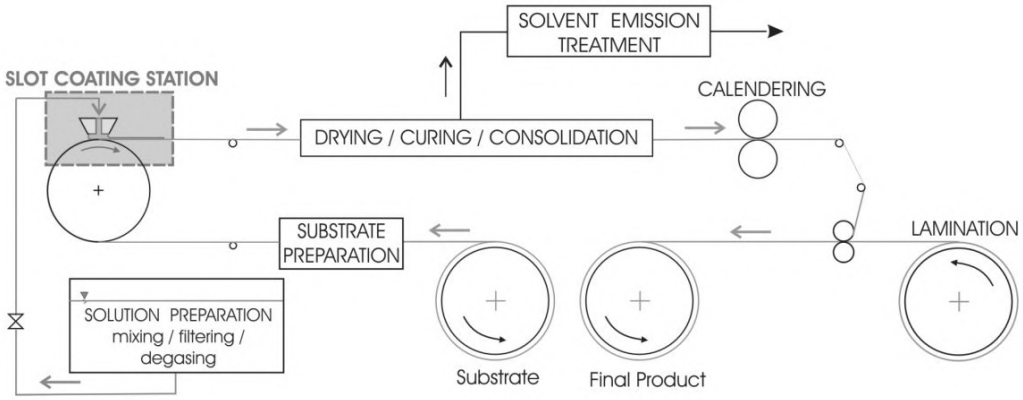

Figure 1.1: Schematic representation of a coating line. (PEREZ; CARVALHO, 2007)

The process starts with the substrate preparation stage. This might involve cleaning the substrate to remove any contaminants that could affect the adhesion of the coating. In some cases, the substrate may also undergo corona treatment to improve its wettability, facilitating even coating spread.

The following stage is liquid preparation, where the coating materials are prepared and conditioned according to the desired properties. This might involve mixing different components, filtering out any impurities, and adjusting the fluid rheology. This stage is very important, since it determines fluid's viscosity behavior expected for the coating stage inlet.

The coating stage is where the prepared liquid is deposited onto the moving substrate. Figure 1.1 shows a slot coating station, which is a common

setup for applying a uniform layer of coating. In slot coating, the liquid is fed through a narrow slot (or die) and then onto the substrate. The thickness of the coating is controlled by the gap between the die and the substrate, as well as the flowrate of the liquid and the moving substrate velocity.

Once the coating has been applied, it needs to be solidified or cured. This can be achieved through various methods, such as heat drying or using a chemical reaction to harden the coating. Sometimes, a final step is needed, which may involve additional post-treatment processes. For instance, calendaring can be used to smooth out the surface of the coating, while lamination involves bonding another layer of material to the coated substrate. The specific post-treatment steps will depend on the desired properties of the final product.

Coating process is applied in the manufacturing of many different products, like paper, magnetic media, adhesive tapes, photographic films, and flexible electronic circuits (PEREZ; CARVALHO, 2007). Moreover, coating is essential for manufacturing high-quality products in automotive, aerospace, electronics, medical, and packaging sectors, ensuring durability, performance, and aesthetics.

There are different types of coating processes commonly used in industrial settings, some examples are blade-, slot-, slide-, extrusion-, curtain-, and roll-coating (KISTLER; SCRIVEN, 1983). Each of those are more suitable for specific applications and substrate characteristics. Curtain coating, for example, is more applied to objects with complex geometries, while slot coating is usually applied for flat substrates, specially in applications that require high thickness accuracy,

Slot coating is distinguished in this last domain of applications due to its unique benefits compared to other methods. A key advantage lies in the ability to generate extremely consistent and accurate coverage over surfaces of a large variety of materials. Slot coating allows for precise management of coating thickness, guaranteeing uniform distribution across the substrate surface. This level of precision is especially crucial in applications where consistent coating is vital for the performance of the end product, such as in producing functional films or electronic coatings.

Another significant advantage of slot coating is offering a notable benefit in terms of material efficiency. With its precise control over a liquid film application, slot coating minimizes waste, leading to more effective use of resources and lower production costs. Furthermore, it is adaptable to a diverse range of liquids, including solvents and particle suspensions, making it suitable for several industrial purposes.

However, despite its many benefits, slot coating also presents specific

challenges to optimize its efficiency and suitability for industrial settings. Die design is one of those challenges, especially in applications involving non-Newtonian liquids. Optimizing coating die geometry to ensure uniform liquid distribution across the substrate width requires a deep understanding of process hydrodynamics and precise fluid flow modeling.

Furthermore, precise control of process conditions, such as substrate speed and liquid flow rate, is essential to ensure consistent coating quality. Variations in process conditions can significantly affect coating thickness and uniformity, underscoring the importance of robust process control systems and continuous product quality monitoring.

The design of the slot coating die is critical to the process success, as it directly determines the coating liquid flow behavior and consequently the film thickness uniformity. Different die geometries are used in the industry, such as T-dies, coat-hanger dies, and fishtail dies, as illustrated in Figure 1.2, each with distinct advantages depending on specific application requirements. The primary goal in die design is to ensure a uniform distribution of coating fluid across the substrate entire width, while also minimizing pressure losses and avoiding flow instabilities like streaks or air entrainment.

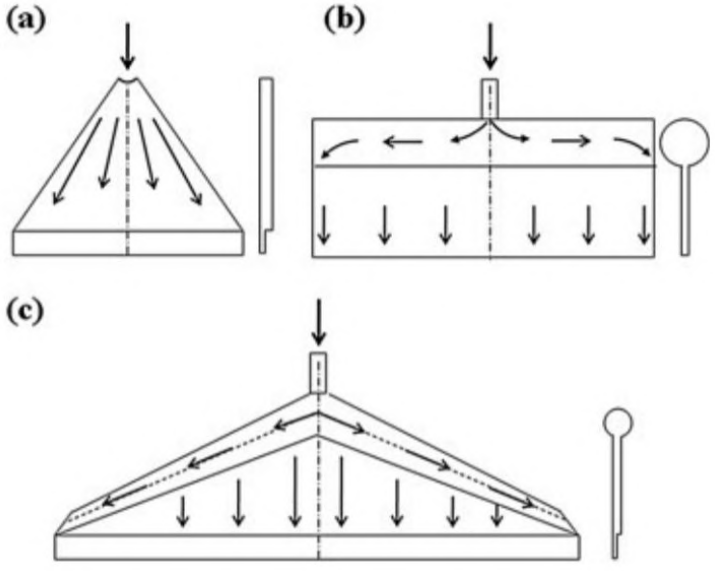

Figure 1.2: Different types of slot coating dies: (a) fishtail die, (b) T-die, (c) coat-hanger die. (LIN et al., 2013)

The flow analysis through the internal passages of coating die manifolds can be divided into four key sections, as illustrated schematically in Figure 1.3(SECOR, 1997):

- Feeding of the cavity,
- Flow through the cavity,

– Flow through the cavity-slot transition, and

– Flow through the slot region.

Proper design and analysis of these flow sections are essential for achieving uniform coating thickness and avoiding common defects.

Geometric parameters are also important for achieving uniformity. The design variables of the die, including die lips, cavity and feed slot dimensions, shape, and inclination, help regulating flow distribution. Precise adjustments in gap clearance and die lips position can minimize flow irregularities, ensuring a smooth coating application. Variations in die geometry can disrupt the flow, leading to non-uniformities in the coating layer, especially at high speeds.

Operating parameters such as web speed, coating thickness and flow rate also contribute to the uniformity of the coating. Maintaining a consistent web speed and feed flow rate helps ensure a stable coating bead and film thickness.

Finally, coating fluids properties, such as viscosity and surface tension, directly impact flow behavior and represent a great modeling challenge in die design. In many applications, complex fluids like emulsions and particle suspensions need to be coated with precise thickness. Non-Newtonian fluids like these, which often exhibit time-dependent behavior, require attention, as their response to shear forces can vary across the coating width causing non-uniform flow profile.

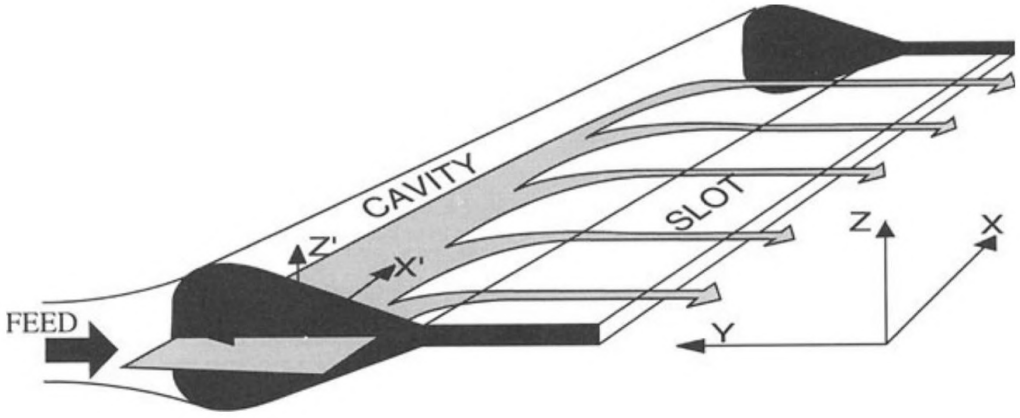

Figure 1.3: Schematic diagram of the general flow pattern in a coating die manifold. (SECOR, 1997)

Lin et al. (2013) proposed a novel design for a coating die specifically aimed at delivering suspensions while addressing common issues such as particle sedimentation and flow uniformity. The design incorporates two easily replaceable shims that allow for adjustments to maintain high shear rates, which is essential for preventing particle sedimentation inside the die. The authors

combined a one-dimensional lubrication approximation with three-dimensional finite element simulations to optimize the die's geometry, ensuring uniform flow across the width of the die. Bingham model was applied to describe the coating suspension behavior, which included viscoplastic characteristics. Experimental validation using three different die designs (T-die, fishtail die, and coat-hanger die) confirmed that the coat-hanger die offered the best performance in terms of flow uniformity and minimizing particle sedimentation.

1.2 Particle suspensions and their non-Newtonian and thixotropic behavior

Particle suspensions are comprised of minute solid particles dispersed within a liquid phase, the interaction between the particles may lead to complex behavior. Many of these structured fluids are commonplace in everyday scenarios, such as mud or blood. Ranging in size from 1 nanometer to 1 micrometer, these particles form colloidal systems. Within colloidal systems, the particles are sufficiently small to remain suspended without rapidly precipitating.

These particle suspensions have wide-ranging applications across various industries. In the coating realm, they play an indispensable role in paints and varnishes, ensuring uniform application. In the cosmetic industry, they are present in creams and lotions, augmenting both texture and spreadability. Within pharmaceuticals, they facilitate the formulation of medications containing insoluble active ingredients, thereby enhancing medication bioavailability. In the lithium-ion battery sector, these suspensions are instrumental in the fabrication of electrode materials, thereby contributing to energy efficiency. In the food sector, they aid in maintaining homogeneity and consistency in products such as sauces and beverages.

In a Newtonian fluid, stress and strain rate maintain a linear relationship, with viscosity dependent solely on pressure and temperature. In contrast, the microstructure of structured fluids, composed of suspended particles dispersed within a liquid phase, stabilizes after prolonged exposure under constant stress conditions, exhibiting distinctly non-Newtonian mechanical behavior.

The response of structured fluids to stress changes can be categorized into two distinct types: instantaneous and time-dependent. In the case of instantaneous response, the fluid's microstructure immediately adjusts to the new stress conditions, reaching equilibrium without any temporal delay. However, for many structured fluids, the transition to a new equilibrium state takes place over time, exhibiting time-dependent behavior.

1.2.1 Time-independent fluids

Figure 1.4 presents different types of non-Newtonian fluid behaviors that exhibit a time-independent response. These include fluids without yield stress, such as pseudoplastic and dilatant fluids, as well as those with yield stress, such as Bingham and Herschel-Bulkley fluids.

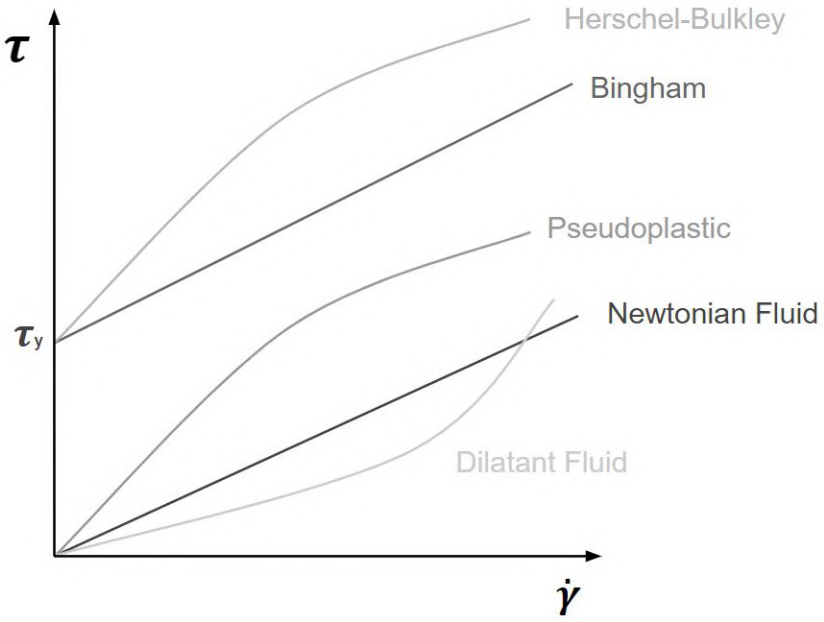

Figure 1.4: Different types of fluid behaviors.

Pseudoplastic fluids, also known as shear-thinning fluids, decrease in viscosity with increasing shear rate. This means that as the fluid is subjected to shaking or shearing, it becomes less viscous. Dilatant fluids, or shear-thickening fluids, increase in viscosity with increasing shear rate. This behavior is the opposite of pseudoplastic fluids; the more they are subjected to shaking or shearing, the thicker and more resistant to flow they become.

Bingham fluids exhibit a yield stress that must be exceeded before they begin to flow. Below this yield stress, they behave like a solid, and above it, they flow like a viscous fluid. Herschel-Bulkley fluids represent a generalized form of Bingham fluids. They display a yield stress and a non-linear relationship between shear stress and shear rate once the yield stress is surpassed. This means they require an initial force to start flowing, but their viscosity also changes in a non-linear fashion with the applied shear rate.

Despite being commonly used, Power-law, Bingham and Herschel-Bulkley models present some limitations while modeling particle suspensions. The Power-law model, for example, can lead to numerical issues, such as predicting infinite viscosity at low shear rates and very low viscosities at high

shear rates. On the other hand, the Bingham and Herschel-Bulkley models may deviate from experimental results depending on particle concentration, as they lack a smooth transition between the solid-like and fluid-like states.

In this study, a viscosity model proposed by Mendes e Dutra (2004) was adopted to describe the rheological behavior of yield-stress fluids. The relation between shear stress and shear rate is defined as the Equation 1-1.

$$\tau = (1 - exp\,(-\eta_0\dot{\gamma}/\tau_0))\,(\tau_0 + K\dot{\gamma}^n) \tag{1-1}$$

where, τ_0 is the yield stress, η_0 is the zero-shear-rate viscosity, $\dot{\gamma}$ is the shear rate, K is the consistency index, and n is the power-law index.

This model addresses the shortcomings of traditional models by introducing a continuous viscosity function, ensuring smooth transitions at the yield stress point. This is crucial for accurately capturing the behavior of yield-stress fluids, which typically exhibit a high viscosity plateau at low shear rates, followed by a sharp viscosity drop once the yield stress is surpassed. By providing this smooth transition, the model better represents the rheological behavior of yield-stress fluids across a wide range of shear rates.

The advantages of this viscosity model is its ability to improve convergence in numerical solutions, particularly in complex flow simulations involving yield-stress fluids. Traditional models often present challenges due to discontinuities or predictions of infinite viscosity at low shear rates, leading to numerical instabilities and inaccurate results. In contrast, the proposed model is continuous, with smooth derivatives, ensuring a stable transition between different flow regimes and minimizing the risk of numerical errors.

This model is suitable for numerical simulations as it eliminates the need for regularization, further enhancing computational efficiency. At extremely low and high shear rates, it accurately predicts the Newtonian plateau, a behavior commonly observed in experimental studies of viscoplastic materials, offering a more precise and reliable representation of their rheological properties in practical applications.

1.2.2 Time-dependent fluids

If a new equilibrium condition is not reached instantly after a step change in stress, the structured fluid is considered time-dependent. Time-dependent fluids exhibit a behaviors where their flow properties change over time under constant shear. These fluids are characterized by viscosity variations that are not solely dependent on the applied shear stress, but also on the time since the change in flow condition. Two common phenomena associated with time-

dependent fluids are thixotropy and rheopexy.

Thixotropy, in particular, is the focus of this research, since there is a wide range of thixotropic fluids present in slot coating processes. These fluids exhibit a shear-thinning behavior, which implies that the fluid's resistance to flow diminishes under higher shear forces. Remarkably, the viscosity change observed in thixotropic fluids is reversible, meaning that the fluid regains its original viscosity upon returning to the original flow condition.

Thixotropy was first defined in the early 20th century by Péterfi (1927) as a mechanically induced sol-gel transition. The term itself is derived from the Greek words thixis (stirring, shaking) and tropos (turning, changing). Over time, the concept of thixotropy has evolved to encompass a broader range of viscosity changes in response to shear forces, particularly in materials that experience a reversible breakdown and recovery of their internal structure.

The studies by Mewis (1979) and Barnes (1997) were instrumental in shaping the modern understanding of thixotropy as a time-dependent, reversible process. These studies showed that under shear, a material's microstructure breaks down, reducing its viscosity, and upon removal of the stress, the structure reforms and viscosity is restored. More recent work by Larson e Wei (2019) highlights the significance of thixotropy in a variety of industrial materials, such as drilling fluids, paints, and many biological substances.

Figure 1.5 illustrates the structural changes in a thixotropic material as it undergoes shear and rest phases. Initially, the fluid is completely structured, giving it an elastic, solid-like response. As shear is applied, the internal structure begins to break down, transitioning to a partially structured state that exhibits viscoelastic behavior. When the structure is completely broken down under shear, the material displays a viscous, shear-thinning response. Once the shear is removed and the fluid is allowed to rest, the structure gradually reforms, eventually returning to its fully structured state, restoring its original viscosity.

This behavior is central to the processing and application of various materials, particularly in processes where control over flow and material stability is essential, such as the coating process. Larson e Wei (2019) offer a comprehensive contribution on how thixotropy manifests in other practical applications, ranging from the flow and setting of paints to the handling of drilling fluids. The structural breakdown that occurs under stress leads to a time-dependent drop in viscosity, also observed in the processing of minerals, metals, food products, pharmaceuticals, ceramics, gels, inks and concrete (JAN; WAGNER, 2009).

In some applications thixotropic behavior is essential, allowing the ma-

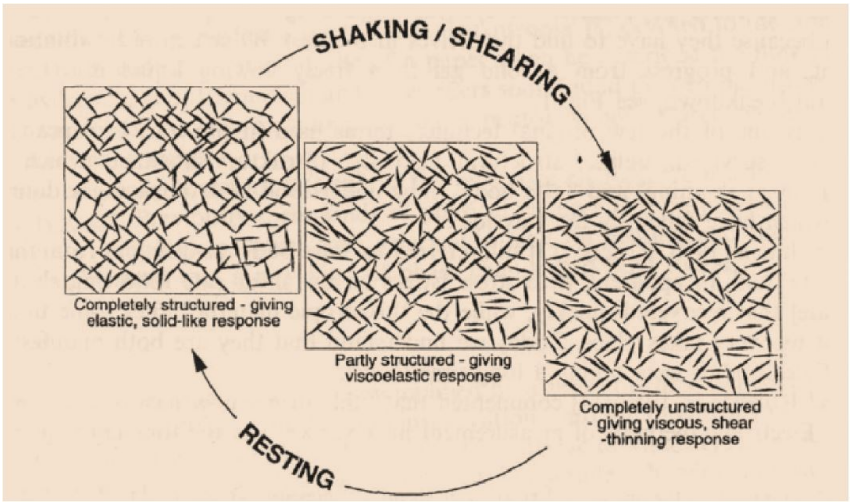

Figure 1.5: Breakdown and build-up of a 3D thixotropic structure. Adapted from Barnes (1997).

terials to flow easily under shear but regaining its stability when at rest. For instance, in the case of paints and other coatings, the material must be easy to apply, flowing smoothly during application, but must also maintain its position and not sag once the application is complete. Similarly, in drilling operations, thixotropic drilling fluids are used to maintain wellbore stability by controlling the flow and recovery of the material's viscosity under different shear conditions.

However, accurately modeling thixotropic materials presents significant challenges. Mendes e Thompson (2012) highlight the need for improved models that account for the combined effects of elasticity, plasticity, and thixotropy, particularly in materials with yield stress. Larson e Wei (2019) suggest that further advancements in microscopic models could help link phenomenological equations with observed behaviors, providing more accurate predictions for industrial applications.

Understanding and controlling the time-dependent properties of thixotropic materials is critical for optimizing performance across a variety of industries. With ongoing research focused on better modeling and measurement techniques, industries will be able to harness the unique properties of thixotropic fluids more effectively, improving product quality and process efficiency.

1.3 Current solutions of slot coating flow

Coating liquids encompass a diverse range of substances, spanning from pure compounds to complex formulations such as polymeric solutions, colloidal

dispersions, particle suspensions, liquid crystals, and melts. It is noteworthy that the majority of these liquids exhibit non-Newtonian behavior, characterized by their intricate rheological properties. Among the pantheon of non-Newtonian fluids, thixotropic fluids emerge as particularly significant players in slot coating processes.

The works of MATSUBARA (MATSUBARA, 1979; 1980; 1983) present one-dimensional models for the flow within coat-hanger dies, focusing on residence time distribution and flow uniformity. These models treat the flow in the manifold and the slot as independent, neglecting any direct interaction between the two. In Matsubara (1979), the initial analysis of the coat-hanger die flow aimed to optimize die geometry, ensuring flow uniformity and reducing residence time. In Matsubara (1980), this analysis is extended to T-dies, where the author proposed general equations for residence time distribution and suggested ways to optimize die geometry. Lastly, in Matsubara (1983), the author studied linearly tapered coat-hanger dies, demonstrating how adjustments to the manifold and slot geometry can maintain flow uniformity without considering interactions between the manifold and slot flows.

Liu, Liu e Tsou (1994) propose a unified lubrication approach combined with one-dimensional lubrication approximation for the design of a coat-hanger die. Using this approximation, the authors have developed general equations for predicting flow uniformity and pressure distribution inside the die, while considering non-Newtonian fluids, including power-law, Ellis, and Bingham models.

In Yu e Liu (1998), the authors combined the one-dimensional lubrication approximation with three-dimensional finite element simulations to optimize the design of an extrusion die using the Carreau fluid model, which accounts for the shear-thinning behavior of non-Newtonian fluids. The lubrication approximation simplifies the analysis by assuming that the fluid motion is locally fully developed and can be considered one-dimensional in both the manifold and the slot section.

Huang, Gentle e Hull (2004) developed an approach to optimize the design of coat-hanger dies using three-dimensional finite element simulations. The study focused on improving flow uniformity in the die, employing the Carreau-Yasuda model to describe the non-Newtonian behavior of the polymer melt.

Han e Wang (2012) used a combination of the orthogonal array design method and numerical simulations to optimize the geometry of a coat-hanger die, focusing on achieving uniform outlet velocity and minimal residence time. The investigated parameters include the manifold angle, the land height, and

the slot gap, all of which significantly affect the flow characteristics. The study utilizes three-dimensional simulations of non-isothermal polymer flow, modeled using the Carreau fluid model, to obtain velocity and residence time profiles across the die. The results show that the manifold angle and slot gap had the most significant impact on both the outlet velocity and residence time, whereas the land height has a smaller influence. While minimizing residence time is critical for reducing thermal degradation of polymers, this approach could pose challenges when dealing with thixotropic materials. Thixotropic polymers require sufficient residence time under shear to fully develop their structure, and minimizing the residence time can lead to inaccurate flow predictions, as the fluid structure does not adjust instantaneously to changes.

Current solutions for analyzing flow in slot coating processes often simplify the problem to make it more manageable and reduce computational costs. Many models adopt one- or two-dimensional flow approximations, treating the flow within the manifold and slot independently, which simplifies interactions between these regions. Another common assumption is to consider the fluid as time-independent, meaning its viscosity depends solely on shear rate, using non-thixotropic models like the Carreau or power-law to describe the fluid rheological behavior.

This approach disregards experimental results obtained for some coating fluids where viscosity decreases under sustained shear and gradually recovers once the shear is removed. By neglecting thixotropy, these models also assume the fluid's internal structure adjusts instantly to changes in the shear field.

Neglecting thixotropy in slot coating models can lead to significant inaccuracies in predicting the uniformity and stability of the coating layer. Without accounting for the time-dependent changes in viscosity, models may fail to capture fluid's response to shear over time and indicate misleading velocity profiles at the die exit. Bad die designs based on poor modeling, may lead to non-uniform outlet velocities, which can create inconsistencies in the coating thickness across the substrate, with some areas receiving more or less material than intended.

Overlook time-dependent behavior can also lead to flow instabilities within the coating layer, as variations in viscosity are not accurately represented. These instabilities may results in defects as streaks, waves, or uneven spreading, which compromise the quality of the coated surface.

Figure 1.6 shows a simplified representation of the flow dynamics within a slot coating die, illustrating two different flow regions: the distribution chamber and the slot. The distribution chamber, which ensures fluid distribution across the width of the die, has its geometry usually simplified by a circular cross-

section area. Hence, the flow in this region can be described using the Poiseuille flow along a tube according to the Equation 1-2.

$$Q(z) = \frac{\pi D^4}{128\mu}\left(-\frac{dp}{dz}\right) \tag{1-2}$$

where $Q(z)$ is the volumetric flow rate at each position z, D is the diameter of the circular cross-section, μ is the viscosity of the fluid, and $-\frac{dp}{dz}$ is the pressure gradient along the tube.

After passing through the distribution chamber, the fluid enters the slot, where it flows between two parallel plates. The flow in this region is governed by the Poiseuille flow between parallel plates, as described in Equation 1-3

$$q_x = \frac{H^3}{12\mu}\left(-\frac{dp}{dx}\right) \tag{1-3}$$

where q_x represents the flow rate per unit width, H is the slot height, μ is the viscosity, and $-\frac{dp}{dx}$ is the pressure gradient across the slot length.

These two descriptions are coupled such that the variation of the flow rate along the cavity is equal to the flow rate through the slot, i.e., $\frac{dQ(z)}{dz} = -q_s(z)$.

Flow in both regions — distribution chamber and slot — is highly dependent on the fluid's viscosity, therefore an accurate rheological model is necessary to predict the fluid behavior under shear. Inaccuracies in modeling viscosity or pressure gradients can lead to variations in the slot outlet velocity profile.

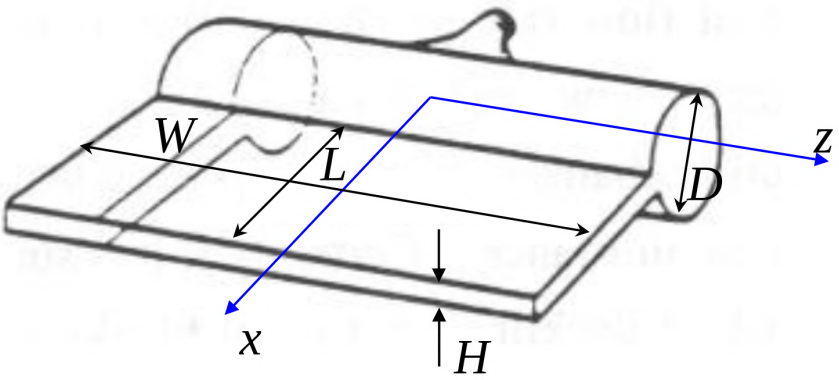

Figure 1.6: Simplified representation of the flow within a slot coating die.

In order to drive liquid towards the end of the distribution chamber, the pressure at the center needs to be higher than the pressure in the end. If the slot length is constant, this would lead to a larger flow rate at the center, leading to a non-uniform coating. To address this issue, the industry has adopted two different strategies: the infinite cavity design, whose objective is to make the pressure drop along the chamber negligible compared to the pressure drop across the slot; and the coat-hanger die, at which the higher

pressure difference along the slot at the center of the die is compensated by a longer slot at the center.

The infinite cavity design achieves a more-or-less uniform flow by significantly increasing the cross-sectional area of the distribution chamber. As described by Equation 1-2, where the diameter of the distribution chamber is raised to the fourth power, even small increases in the chamber's diameter lead to a substantial reduction in the pressure drop along the chamber. Consequently, any small variation in the pressure difference within the distribution chamber is sufficient to drive the flow sideways. By making the pressure inside the cavity much higher than the outlet pressure, these small pressure differences become negligible, resulting in smaller variations of the average velocity throughout the feed slot width.

Therefore, this design employs a large cross-section of the distribution chamber and operates at higher pressures within the cavity, reducing the influence of the pressure drop along the chamber compared to the pressure drop across the slot. However, this approach requires that the die be constructed from materials strong enough to resist elastic deformation due to the high pressure in the cavity. This requirement leads to the use of larger dies, which increases production costs and makes the system less economical.

Despite these drawbacks, the infinite cavity design offers a significant advantage by serving a wide range of viscosities and flow rates, which makes it a robust solution for handling thixotropic fluids. By ensuring uniform pressure and flow distribution, this design effectively compensates for the time-dependent viscosity changes inherent in thixotropic materials. Although the higher costs and material demands are disadvantages, the ability to achieve uniform coatings even with challenging fluid properties makes this the preferred approach in many industrial applications.

In contrast, instead of increasing the cross-sectional area of the distribution chamber, the coat-hanger die modifies the length of the feed slot across its width. In essence, the slot at the center of the die is extended relative to the ends, creating a pressure drop distribution that compensates for the higher flow rate tendency near the middle. Thus, even though the pressure may be higher in the center of the chamber, the longer slot region there forces the fluid to traverse a longer path before exiting. This extended flow path balances the flow distribution, resulting in a more uniform flow.

In contrast to the infinite cavity design, which accommodates a broad range of fluid behaviors by relying on large chamber cross-sections and high operating pressures, the coat-hanger die uses a more geometrically tuned approach. Rather than allowing the chamber's diameter to dominate the

pressure drop, the slot at the center of the die is extended relative to the ends, creating a pressure drop distribution that compensates for the higher flow rate tendency near the middle. Thus, even though the pressure may be higher in the center of the chamber, the longer slot region there forces the fluid to traverse a longer path before exiting. This extended flow path balances the flow distribution, resulting in a more uniform flow without the extreme pressures required by an infinite cavity. Consequently, the coat-hanger die can be made smaller and lighter, consuming fewer materials and reducing overall production costs.

However, this design strategy also places demands on the rheological modeling of the fluid in question. While the infinite cavity design make it robust for various complex fluids—including tixotropic ones—the coat-hanger die must be customized for a specific rheology. If the actual fluid differs significantly from the model used the flow can become uneven and yield a suboptimal coating.

Despite these challenges, the coat-hanger die remains a used solution when the target fluid's properties are well-known. Industries that work with a single or limited set of rheologically similar fluids can benefit from this design strategy, trading the extra material and operating pressure demands of the infinite cavity for a more compact, cost-effective design. However, manufacturers must ensure their rheological models are reliable and account for the fluid's time-dependent.

1.4 Objectives

The study aims to develop a model that accounts for the thixotropic effects in the design of the cavity of a coating die by numerically simulating the three-dimensional flow of thixotropic fluids. By integrating the time-dependent behavior of thixotropic fluids, the objective is to achieve more precise flow predictions and a better understanding of how these properties influence the pressure distribution and velocity profile within the coating die. The study seeks to match falling pressure along the distribution chamber with decreasing pressure drops down a shortening slot.

Accounting for time-dependent behavior allows the design of a distribution chamber with smaller cross-sectional area, which reduces material requirements and operational challenges associated with high-pressure systems. It targets achieving lower pressures within the cavity, lowering the overall cost of die manufacturing while maintaining the uniformity of the coating process.

The study focused on developing a three-dimensional thixotropic fluid

model within a finite element method framework. The simulations were conducted using a Fenics-based approach. This aimed to provide insights into the interaction between the fluid's thixotropic properties and the die geometry, offering a more cost-effective alternative to current industrial solutions like the infinite cavity design.

1.5 Outline

This dissertation is divided into six chapters.

In Chapter 1, the coating process is introduced, with a focus on slot coating and its industrial applications. The chapter also discusses the challenges of coating particle suspensions, particularly their non-Newtonian and thixotropic behavior, and reviews current modeling approaches and their limitations.

Chapter 2 presents the mathematical model used to describe thixotropic fluid flow. It covers the thixotropic model, conservation equations, and the nondimensionalization process to simplify the governing equations for numerical simulations.

Chapter 3 details the numerical simulation methodology. It includes the weak formulation of the governing equations, the finite element method, mesh definition, boundary conditions, and the solution procedure using the FEniCS framework.

In Chapter 4, the three-dimensional flow in a slot coating die is analyzed. The geometric and rheological properties of the die are described, along with the boundary conditions and mesh convergence analysis used to ensure accurate simulations.

Chapter 5 presents the simulation results, comparing the flow behavior predicted by the Generalized Newtonian Model (GNM) and the thixotropic model. The effects of thixotropy on velocity, pressure, and fluidity fields are discussed, along with the impact of geometric modifications on flow uniformity.

Finally, Chapter 6 summarizes the conclusions of the study, emphasizing the importance of considering thixotropic effects in die design. It also suggests future work, such as rheological characterization of battery slurries and further optimization of die geometries.

2
Mathematical model

2.1
Thixotropic fluids and the thixotropic model

Mendes, Abedi e Thompson (2018) presents a groundbreaking constitutive model for elastoviscoplastic thixotropic materials. This model significantly departs from existing approaches by establishing a direct relationship between the material's microscopic state and fluidity (ϕ_v), which is the reciprocal of the viscosity (FREDRICKSON, 1970). Consequently, the fluidity itself is used as a measure of the microscopic state, eliminating the need for a structure parameter (λ) in the formulation.

$$\phi_v = \frac{1}{\eta_v} \tag{2-1}$$

Furthermore, the researchers introduce a novel evolution equation for fluidity. This equation stands out for its reliance solely on measurable material functions, that are measurable by standard rheological experiments, avoiding any postulated functions or parameters. To connect stress and kinematics, the study employs a tensorial Oldroyd-B-like differential equation. The relaxation and retardation times within this equation are also derived from measurable functions of fluidity.

The mechanical response of the liquid is depicted in Figure 2.1, where it is assumed that the material follows a Jeffreys analog. Accordingly, the fluidity can be defined by Equation 2-2.

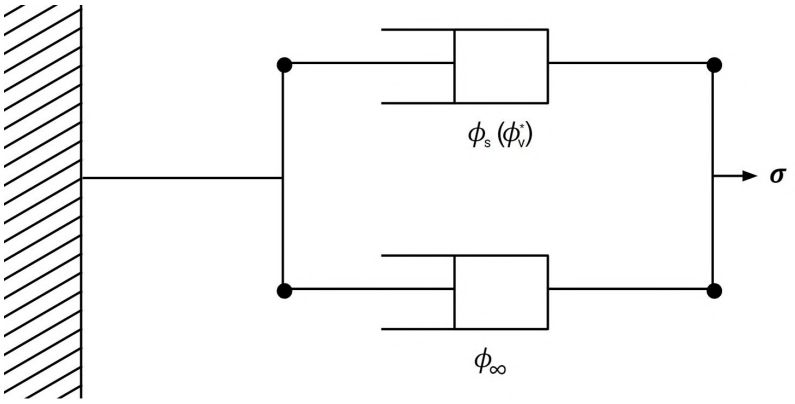

Figure 2.1: Mechanical response of a liquid modeled using a Jeffreys analog.

$$\frac{1}{\phi_v} = \frac{1}{\phi_s} + \frac{1}{\phi_\infty} \tag{2-2}$$

where ϕ_v represents the current fluidity, ϕ_s denotes the structural fluidity, and ϕ_∞ indicates the fluidity when the fluid is fully unstructured, which is also the maximum possible value of ϕ_v. As conditions approach full fluid unstructuring, ϕ_v asymptotically tends towards ϕ_∞. There is also a minimum value for ϕ_s that denotes the fluidity of a fully structured fluid, referred to as ϕ_0. Thus, incorporating both the upper and lower limits of ϕ_v, a normalized fluidity (ϕ_v^*) is defined in Equation 2-3.

$$\phi_v^* = \frac{\phi_v - \phi_0}{\phi_\infty - \phi_0} \tag{2-3}$$

Therefore, $\phi_v^* = 0$ corresponds to the highest level of structuring, indicating a fully structured state of the material. In contrast, $\phi_v^* = 1$ corresponds to the lowest level of structuring, indicating a fully unstructured state. The rate of change of the level of structuring is influenced by the current fluidity and stress intensity. This relationship is described by the following evolution equation, which governs how the structuring evolves over time based on these parameters:

$$\frac{\partial \phi_v^*}{\partial t} + \vec{u} \cdot \nabla \phi_v^* = f(\sigma, \phi_v^*) \tag{2-4}$$

where $\vec{u}$ represents the velocity vector field, σ is the current stress intensity, given by $\sigma = \eta\dot{\gamma}$ with $\dot{\gamma} = \sqrt{2(\bar{\bar{D}} : \bar{\bar{D}})}$.The deformation tensor $\bar{\bar{D}}$ is defined as $\bar{\bar{D}} = \frac{1}{2} \cdot (\nabla\vec{u} + (\nabla\vec{u})^T)$.

In steady-state flow conditions, $f(\sigma, \phi_v^*) = 0$, and the fluidity ϕ_v^* is assumed to reach equilibrium, denoted as $\phi_{eq}^*(\sigma)$. Since this equilibrium fluidity is solely a function of the current stress, the dependence on f can be replaced, and the evolution equation for ϕ_v^* can be written as in Equation 2-5.

$$\frac{\partial \phi_v^*}{\partial t} + \vec{u} \cdot \nabla \phi_v^* = f(\phi_{eq}^*(\sigma), \phi_v^*) \tag{2-5}$$

Thus, the dimensionless equilibrium fluidity can be expressed as in Equation 2-6.

$$\phi_{eq}^*(\sigma) = \frac{\left[\frac{1}{\sigma}\left(\frac{\sigma}{K}\right)^{\frac{1}{n}}\right]}{(\phi_\infty - \phi_0) + \left[\frac{1}{\sigma}\left(\frac{\sigma}{K}\right)^{\frac{1}{n}}\right]} \tag{2-6}$$

where K represents the consistency index, n is the power-law index, the expression includes Newtonian plateaus ϕ_0 and ϕ_∞ at both ends of the stress range, characterizing the fluidity under low and high-stress conditions, respectively. In this study, the model neglects yield stress σ_y. Equation 2-6, derived from the Herschel-Bulkley equation, was used to fit the steady-state data from a laponite suspension. It accurately reflects the behavior of the model within the range of intermediate stresses, excluding the Newtonian plateaus.

This equilibrium fluidity is measured during a very common rheological experiment that allows to determine the steady-state or equilibrium viscosity (η_{eq}) as a function of the shear rate ($\dot{\gamma}$). These experiments are necessary for understanding the material's rheological properties, as they provide insight into how the fluid behaves under various stress conditions. The relationship between equilibrium viscosity and equilibrium fluidity is given by Equation 2-1, allows the data to be expressed in terms of normalized fluidity (ϕ^*_{eq}).

Achieving a steady-state condition is particularly important for time-dependent fluids, which may exhibit transient behaviors before reaching equilibrium. Sufficient time must be allowed during experiments to ensure that the fluid has fully responded to the applied stress and that no further changes in fluidity or shear rate are occurring. This ensures the accuracy and reliability of the measured data, which is crucial to determine the rheological characteristics of the fluid.

Based on the construction and destruction experimental data collected by Mendes, Abedi e Thompson (2018), an evolution equation for a laponite suspension consistent with the experimentally observed behavior was proposed. This equation, represented by Equation 2-7, captures the dynamics of buildup and breakdown of the suspension's liquid structure.

$$f(\phi^*_{eq}, \phi^*_v) = \begin{cases} \frac{s}{t_a \cdot \phi^*_{eq}} (\phi^*_{eq} - \phi^*_v)^{\frac{s+1}{s}} {\phi^*_v}^{\frac{s-1}{s}}, & 0 < \phi^*_v \leq \phi^*_{eq} \\ -\frac{\phi^*_v - \phi^*_{eq}}{t_c}, & \phi^*_{eq} < \phi^*_v \leq 1 \end{cases} \tag{2-7}$$

In the first case, when $0 < \phi^*_v \leq \phi^*_{eq}$, the microstructure undergoes breakdown, where s is a positive parameter and t_a represents the avalanche time. The second case, when $\phi^*_{eq} < \phi^*_v \leq 1$, the microstructure builds up, where t_c is the construction time. In this study, the parameters for construction time and avalanche time will be modified to understand their influence on thixotropy. Specifically, varying these parameters aims to analyze how the fluid's microstructure behaves under different time conditions. Since the fluid being studied does not exist in reality, the focus is on examining the impact of these characteristic times on thixotropy, using the parameter s as defined by Mendes, Abedi e Thompson (2018) for a laponite suspension according to the Equation 2-8.

$$s = \frac{8}{\exp\left(\frac{\phi^*_{eq}}{0.09}\right) - 1} + 1.2 \tag{2-8}$$

It is important to mention that different functional forms of $f(\phi^*_{eq}, \phi^*_v)$ can be used, depending on the liquid transient response.

2.2 Conservation equations

Fluid flow is commonly described by mass conservation and momentum conservation equations, which are fundamental to understanding the behavior of flowing fluids. It can be expressed as:

$$\frac{\partial \rho}{\partial t} + \vec{u}.\nabla\rho + \rho\nabla.\vec{u} = 0 \tag{2-9}$$

$$\frac{\partial \rho\vec{u}}{\partial t} + \rho\vec{u}\cdot\nabla\vec{u} = \nabla\cdot\bar{\bar{T}} + \rho\vec{g} \tag{2-10}$$

where, ρ denotes the fluid density, $\vec{g}$ indicates the body forces field (e.g. gravity), and $\bar{\bar{T}}$ refers to the stress tensor. For a viscous fluid, the stress tensor is defined as $\bar{\bar{T}} = 2\eta\bar{\bar{D}} - p\bar{\bar{I}}$, where η stands for the local viscosity of the fluid, p signifies the pressure field,$\bar{\bar{I}}$ is the identity tensor.

When examining the theories of steady-state and incompressible fluid conditions, it is crucial to acknowledge that specific terms are intentionally disregarded due to the incorporation of these assumptions in this research. By adopting steady-state conditions, we ignore the time derivative terms in both the mass conservation and momentum conservation equations $\left(\frac{\partial}{\partial t} = 0\right)$. This simplification is warranted when the flow variables remain constant over time, enabling us to concentrate exclusively on spatial changes.

In addition, the assumption of incompressible fluid conditions implies that the density of the fluid stays uniform across the flow domain $\left(\frac{\partial \rho}{\partial} = 0\right)$.

Furthermore, inertial terms are neglected under the assumption that flow velocities are sufficiently low to make acceleration effects insignificant. This simplification applies in situations where the flow is characterized by slow and viscous movement.

Body forces are also neglected ($\vec{g} = 0$), indicating that the impact of gravitational forces on fluid flow is considerably smaller in comparison to other forces.

After making these simplifying assumptions, the mass and momentum conservation equations are simplified to:

$$\nabla\cdot\vec{u} = 0 \tag{2-11}$$

$$\nabla\cdot\bar{\bar{T}} = 0 \tag{2-12}$$

2.3 Nondimensionalization of Equations

Dimensional analysis is a critical technique in mathematical modeling that involves transforming equations into a dimensionless form. In Section 2.2,

the governing equations for mass conservation, momentum conservation, and fluidity were defined in their dimensional forms. To streamline the analysis and facilitate numerical simulations, these equations are transformed into their nondimensional forms. This process is essential for numerical solutions using finite element methods, as it enables the normalization of parameters and standardization of variables. By enhancing the stability and accuracy of numerical methods, dimensional analysis facilitates better convergence of solutions and more effective interpretation of results, increasing the efficiency of finite element algorithms.

In the process of nondimensionalizing equations, scaling parameters are used to define all variables in dimensionless forms. This transformation helps to simplify and standardize mathematical models. Table 2.1 outlines the key scaling parameters, their descriptions, and their primary dimensions.

Scaling Parameter	Description	Primary Dimensions
L_{char}	Characteristic length	m
U_{char}	Characteristic speed	$m \cdot s^{-1}$
$\phi_\infty - \phi_0$	Reference fluidity difference	$m \cdot s \cdot kg^{-1}$

Table 2.1: Scaling parameters used for nondimensionalization, including their descriptions and primary dimensions.

The following equations define the non-dimensional variables using the scaling parameters:

- Velocity: The non-dimensional velocity $\vec{u^*}$ is obtained by normalizing the velocity with the characteristic speed.

$$\vec{u^*} = \frac{\vec{u}}{U_{char}} \tag{2-13}$$

- Pressure: The non-dimensional pressure p^* is defined by scaling the pressure with characteristic length and speed, and the reference fluidity difference.

$$p^* = \frac{p\ L_{char}\ (\phi_\infty - \phi_0)}{U_{char}} \tag{2-14}$$

- Spatial Coordinates and Gradient Operator: The nondimensional spatial coordinates $\vec{x}^*$ and gradient operator $\vec{\nabla}^*$ are obtained by scaling with characteristic length.

$$\vec{x^*} = \frac{\vec{x}}{L_{char}} \tag{2-15}$$

$$\nabla^* = L_{char}\ \nabla \tag{2-16}$$

- Fluidity: The non-dimensional fluidity ϕ^* is defined by normalizing the fluidity as described in Section 2.1. It is scaled by the reference

fluidity difference $\phi_\infty - \phi_0$, where ϕ_∞ represents the fluidity of the fully unstructured fluid, and ϕ_0 denotes the fluidity of the fully structured fluid.

$$\phi^* = \frac{\phi - \phi_0}{\phi_\infty - \phi_0} \tag{2-17}$$

– Time: The non-dimensional time t^* is defined as the ratio of the characteristic speed U_{char} to the characteristic length L_{char}.This results in time being expressed in dimensionless units:

$$t^* = \frac{t\ U_{char}}{L_{char}} \tag{2-18}$$

With these definitions, the equations are now expressed in their nondimensional forms. The next step involves explicitly defining the nondimensional versions of the governing equations for mass conservation, momentum conservation, and fluidity.

Mass Conservation: After the simplifications assumptions, the dimensional mass conservation equation can be written as:

$$\nabla \cdot \vec{u} = 0 \tag{2-19}$$

When transformed into nondimensional form, using the previously defined nondimensional variables, the mass conservation equation becomes:

$$\frac{\nabla^*}{L_{char}} \cdot \vec{u}^* \cdot U_{char} = 0 \tag{2-20}$$

$$\nabla^* \cdot \vec{u}^* = 0 \tag{2-21}$$

Momentum Conservation: The dimensional momentum conservation equation with previous assumptions is expressed as:

$$\nabla \cdot \bar{\bar{T}} = 0 \tag{2-22}$$

To express this equation in its nondimensional form, it is necessary to present it in an explicit form. Specifically, the viscosity term μ is replaced by the fluidity ϕ_v, which is the reciprocal of the viscosity, as defined in Section 2.1. This substitution transforms the momentum conservation equation into:

$$\nabla \cdot \left\{ \frac{\cancel{2}}{\phi_v} \cdot \left[\frac{1}{\cancel{2}} \left(\nabla \vec{u} + (\nabla \vec{u})^T \right) \right] - p\bar{\bar{I}} \right\} = 0 \tag{2-23}$$

$$\nabla \cdot \left\{ \frac{1}{\phi_v} \cdot \left[\nabla \vec{u} + (\nabla \vec{u})^T \right] - p\bar{\bar{I}} \right\} = 0 \tag{2-24}$$

In its nondimensional form, incorporating the scaling parameters, the momentum conservation equation is:

$$\frac{\nabla^*}{L_{char}} \cdot \left\{ \frac{1}{\phi_v^* \cdot (\phi_\infty - \phi_0) + \phi_0} \cdot \left[\frac{\nabla^* \cdot \vec{u}^* \cdot U_{char}}{L_{char}} + \left(\frac{\nabla^* \cdot \vec{u}^* \cdot U_{char}}{L_{char}} \right)^T \right] - \frac{p^* \cdot U_{char}}{L_{char} \cdot (\phi_\infty - \phi_0)} \bar{\bar{I}} \right\} = 0 \tag{2-25}$$

$$\frac{\nabla^*}{\cancel{L_{char}}} \cdot \left\{ \frac{1}{\phi_v^* \cdot (\phi_\infty - \phi_0) + \phi_0} \cdot \frac{\cancel{U_{char}}}{\cancel{L_{char}}} \left[\nabla^* \cdot \vec{u}^* + (\nabla^* \cdot \vec{u}^*)^T \right] - \frac{\cancel{U_{char}}}{\cancel{L_{char}}} \frac{p^*}{(\phi_\infty - \phi_0)} \bar{\bar{I}} \right\} = 0 \tag{2-26}$$

$$\nabla^* \cdot \left\{ \frac{(\phi_\infty - \phi_0)}{\phi_v^* \cdot (\phi_\infty - \phi_0) + \phi_0} \cdot \left[\nabla^* \cdot \vec{u}^* + (\nabla^* \cdot \vec{u}^*)^T \right] - p^* \bar{\bar{I}} \right\} = 0 \tag{2-27}$$

After simplifying the terms of the momentum conservation equation, the nondimensional Equation 2-27 can be expressed in a more compact form as:

$$\nabla^* \cdot \bar{\bar{T}}^* = 0 \tag{2-28}$$

Fluidity Equation: The dimensional equation for fluidity can be divided into two distinct cases, each describing a different behavior of the microstructure.

For the breakdown of microstructure, when $0 < \phi_v^* \leq \phi_{eq}^*$, the dimensional fluidity equation can be expressed as:

$$\vec{u} \cdot \nabla \phi_v^* = \frac{s}{t_a \cdot \phi_{eq}^*} (\phi_{eq}^* - \phi_v^*)^{\frac{s+1}{s}} {\phi_v^*}^{\frac{s-1}{s}}, \quad 0 < \phi_v^* \leq \phi_{eq}^* \tag{2-29}$$

By applying the nondimensional variables, the equation transforms into its nondimensional form:

$$\frac{U_{char}}{L_{char}} \cdot \vec{u}^* \cdot \nabla^* \phi_v^* = \frac{U_{char}}{L_{char}} \frac{s}{t_a^* \cdot \phi_{eq}^*} (\phi_{eq}^* - \phi_v^*)^{\frac{s+1}{s}} {\phi_v^*}^{\frac{s-1}{s}} \tag{2-30}$$

$$\vec{u}^* \cdot \nabla^* \phi_v^* = \frac{s}{t_a^* \cdot \phi_{eq}^*} (\phi_{eq}^* - \phi_v^*)^{\frac{s+1}{s}} {\phi_v^*}^{\frac{s-1}{s}} \tag{2-31}$$

For the build-up of microstructure, when $\phi_{eq}^* < \phi_v^* \leq 1$, the dimensional fluidity equation can be written as:

$$\vec{u} \cdot \nabla \phi_v^* = -\frac{\phi_v^* - \phi_{eq}^*}{t_c}, \quad \phi_{eq}^* < \phi_v^* \leq 1 \tag{2-32}$$

The nondimensional form of this equation is given by:

$$\frac{U_{char}}{L_{char}} \cdot \vec{u}^* \cdot \nabla^* \phi_v^* = -\frac{U_{char}}{L_{char}} \frac{\phi_v^* - \phi_{eq}^*}{t_c^*} \tag{2-33}$$

$$\vec{u}^* \cdot \nabla^* \phi_v^* = -\frac{\phi_v^* - \phi_{eq}^*}{t_c^*} \tag{2-34}$$

In conclusion, the nondimensional fluidity equation is given by:

$$\vec{u}^* \cdot \nabla^* \phi_v^* = \begin{cases} \frac{s}{t_a^* \cdot \phi_{eq}^*} (\phi_{eq}^* - \phi_v^*)^{\frac{s+1}{s}} {\phi_v^*}^{\frac{s-1}{s}}, & 0 < \phi_v^* \leq \phi_{eq}^* \\ -\frac{\phi_v^* - \phi_{eq}^*}{t_c^*}, & \phi_{eq}^* < \phi_v^* \leq 1 \end{cases} \tag{2-35}$$

By converting the governing equations into their nondimensional form, it enables a more generalized analysis of fluid properties such as fluidity and characteristic times. This transformation enhances the efficiency of numerical simulations, especially when employing finite element methods. It improves computational stability and accuracy by nondimensionalization of the variables, which reduces the risk of numerical instabilities and minimizes the sensitivity to small perturbations in the solution. Additionally, it helps balance the scales in the system, preventing disproportionately large or small numbers that can otherwise hinder the precision of numerical solvers. This normalization not only accelerates convergence but also allows for more optimized algorithms, leading to faster and more efficient solutions.

3
Numerical simulation

The presented problem involves a complex set of physical phenomena. Hence, the task of developing a comprehensive analytical model is quite challenging, especially since the system is inherently nonlinear and multivariable. Even in simplified flow scenarios, such as certain two-dimensional Newtonian flows, analytical solutions to the governing partial differential equations (PDEs) may not be feasible. Consequently, the solution requires the aid of numerical methods to accurately solve coupled differential equations.

The Finite Element Method (FEM) emerges as a numerical technique for solving the partial differential equations applied in this context. A computational framework that facilitates FEM implementation is the *DOLFIN* library (LOGG; WELLS, 2010), which provides algorithms for discretizing and solving a wide range of PDEs. In this study, a 3D finite element numerical model has been proposed and implemented in *Python*, using the precompiled *DOLFIN* library, which is developed within the open-source project *FEniCS* (LOGG; MARDAL; WELLS, 2012).

3.1
Weak formulation

This section explores the finite element method, a numerical technique used to solve partial differential equations over complex domains. Central to this approach is to express all the fields, i.e. velocity, pressure and fluidity, as linear combination of basis function and to rewrite the governing equations according to the weak formulation. To derive the weak formulation, each governing equation is multiplied by a corresponding weight function and integrated over the domain Ω, ensuring the solution satisfies the equations in an averaged sense across the entire domain.

For mass and momentum conservation equations, and fluidity equation, the respective weight functions are chosen to reflect the nature of each independent variable: scalar weight functions for mass and fluidity equations; and a vector weight function for the momentum equation. This process leads to the weighted residual method, where the integrated equations are expressed as weighted residuals, capturing the approximation errors across the domain.

The weighted residual for the momentum conservation is shown in Equation 3-1:

$$\int_{\Omega} \left[\nabla^* \cdot \bar{\bar{T}}^*\right] \cdot \vec{v^*}\ d\Omega^* = 0 \tag{3-1}$$

where $\vec{v^*}$ represents the vector weight function for momentum conservation, ensuring that the momentum equation is satisfied in its weak form.

Equation 3-1 can be rearranged using the tensor identity (ARIS, 2012):

$$\nabla \cdot \left(\bar{\bar{A}} \cdot \vec{\xi}\right) = \bar{\bar{A}} : \nabla\vec{\xi} + \left(\nabla \cdot \bar{\bar{A}}\right) \cdot \vec{\xi} \tag{3-2}$$

Applying this identity, Equation3-1 can be written as:

$$\int_{\Omega} \nabla^* \cdot \left(\bar{\bar{T}}^* \cdot \vec{v^*}\right)\ d\Omega^* - \int_{\Omega} \bar{\bar{T}}^* : \nabla^*\vec{v^*}\ d\Omega^* = 0 \tag{3-3}$$

Using the divergence theorem, the equation is written as:

$$\int_{\Omega} \nabla^* \cdot \left(\bar{\bar{T}}^* \cdot \vec{v^*}\right)\ d\Omega^* = \oint_{\Gamma} \left(\vec{n} \cdot \bar{\bar{T}}^*\right) \cdot \vec{v^*}\ d\Gamma^* \tag{3-4}$$

Thus, the weighted residual of the momentum conservation Equation 3-3 can be expressed in a form where second derivative terms of the basis or weight functions do not appear.

$$\oint_{\Gamma} \left(\vec{n} \cdot \bar{\bar{T}}^*\right) \cdot \vec{v^*}\ d\Gamma^* - \int_{\Omega} \bar{\bar{T}}^* : \nabla^*\vec{v^*}\ d\Omega^* = 0 \tag{3-5}$$

These transformations allow easier definitions of certain boundary conditions, which will become clearer in Section 3.4. Analogously, the same process is applied to the mass conservation and fluidity equations, whose strong forms are given by Equation 2-21 and Equation 2-35, respectively. Since these equations do not involve higher-order derivatives of velocity, pressure, or fluidity, the resulting weak formulations are more straightforward. The weighted residuals for the mass conservation and fluidity equations are shown in Equations 3-6 and 3-7.

$$\int_{\Omega} \left[\nabla^* \cdot \vec{u^*}\right]\ q^*\ d\Omega^* = 0 \tag{3-6}$$

$$\int_{\Omega} \left[\vec{u^*} \cdot \nabla^*\phi_v^* - f^*(\phi_{eq}^*, \phi_v^*)\right]\ m^*\ d\Omega^* = 0 \tag{3-7}$$

where q^* and m^* represent scalar weight functions, corresponding to the mass conservation and fluidity equations, respectively. These scalar functions ensure that the residuals for both equations are minimized over the entire domain Ω, just as in the case of momentum conservation.

3.2 Base and Weight Functions

The Navier-Stokes equations exhibit instabilities when velocity and pressure are treated in a coupled manner in the standard Galerkin formulation, using interpolating polynomials of the same order. To mitigate this issue, Tay-

lor and Hood elements are employed. These elements constitute a mixed space where the basis function of the pressure element is linear continuous, while the basis function of the velocity field employs a quadratic continuous element. These elements are chosen to ensure the Ladyzhenskaya-Babuška-Brezzi (LBB) condition, or inf-sup condition, which contributes to the stability and convergence of the method.

For these two unknown fields, the Galerkin Finite Element Method is used. In this method, the weight functions are the same as the basis functions, and they are used to calculate the residual in the weak formulation.

In addition to the velocity and pressure fields, the current problem also depends on the calculation of a fluidity field, for which a linear continuous basis function is used. Unlike the other fields, the Galerkin method is corrupted by non-physical numerical instabilities when the equations are predominantly convective (i.e., with strong hyperbolic terms). One way to avoid this type of instability is to use the Streamline-Upwind/Petrov-Galerkin (SUPG) stabilized formulation (BROOKS; HUGHES, 1982). In this case, the fluidity weighting functions are modified to:

$$m^* = \psi_{\phi^*} + h^U(\vec{v^*} \cdot \nabla\psi_{\phi^*}) \tag{3-8}$$

where ψ_{ϕ^*} is the basis function and h^U is the upwind parameter, which was chosen to match the characteristic size of the smallest element in the computational mesh.

3.3 Mesh definition

Considering the flexibility and adaptability needed to apply local refinement along the problem domain, an unstructured mesh with tetrahedral elements (as shown in Figure 3.1) was used. Tetrahedral elements enable easier modeling of complex geometries compared to other types of three-dimensional elements, such as hexahedrons. Additionally, unstructured meshes assist in this process by effectively filling domains with irregular boundaries and complex geometries, as seen in slot coating applications.

There are numerous efficient and robust algorithms for generating such meshes in complex three-dimensional domains. In this study, Gmsh, an open-source 3D finite element mesh generator, was used (GEUZAINE; REMACLE, 2009). Gmsh employs the Delaunay method, which facilitates mesh creation even on irregular surfaces.

Using this type of algorithm to generate unstructured tetrahedral meshes allows for adaptive refinement. This means increasing the element density in

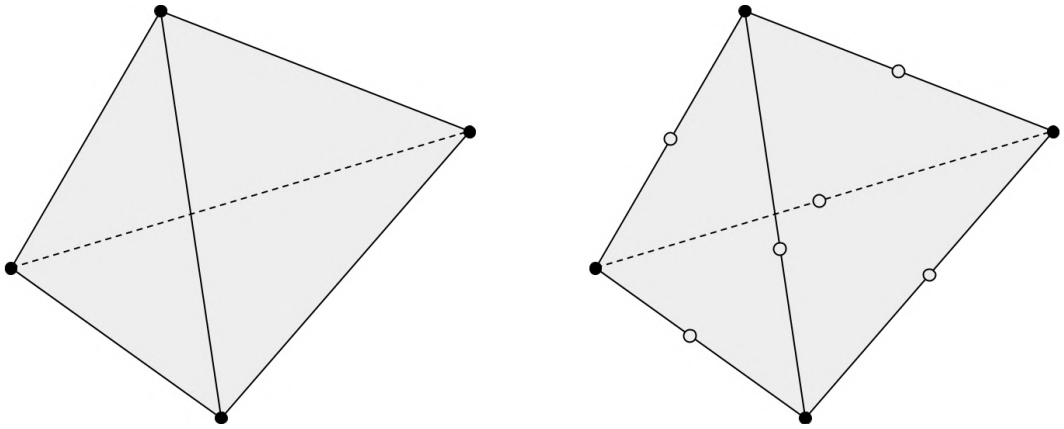

a) Linear 4-node Tetrahedron b) Quadratic 10-node Tetrahedron

Figure 3.1: First and Second Order Mesh Elements.

regions requiring higher precision or where the solution varies rapidly, and using lower element density in regions where the solution is smoother. This approach significantly conserves computational resources.

3.4 Boundary condition

Boundary conditions are a crucial component in the solution of partial differential equations and boundary value problems, providing essential information about the solution behavior at problem's domain edges. They serve as mathematical constraints that define the solution value or derivative value along the boundaries, enabling the determination of unique solutions.

Dirichlet boundary conditions specify the value of a variable on the domain boundary, providing information about the solution's behavior at those locations. Neumann boundary conditions, on the other hand, specify the derivative value of a variable along the boundary. The boundary is divided into four parts in this study, as shown in Figure 3.2.

Figure 3.2: Schematic of the flow domain boundary.

– Inlet boundary: The inlet boundary represents the region where the fluid enters the computational domain. During the simulation, Dirichlet

boundary conditions were imposed at this boundary to define the velocity and fluidity profiles of the inflowing fluid.

$$\vec{u^*}(x) = \vec{g}(x) \quad \forall x \in \Gamma_1$$
$$\phi^*(x) = h(x) \quad \forall x \in \Gamma_1$$

where $\vec{g}$ and h is a known function defined on the boundary Γ_1.

Since these conditions were imposed for velocity, the weighting functions become zero at this boundary, canceling the term on the inlet boundary in Equation 3-5.

$$\Gamma_1 : \left\{ \vec{u^*}(x) = \vec{g}(x) \longrightarrow \oint_{\Gamma_1} \left(\vec{n} \cdot \bar{\bar{T}}^*\right) \cdot \cancelto{0}{\vec{v^*}}\, d\Gamma^* = 0 \right. \tag{3-9}$$

– Outlet boundary: The outlet boundary is the region where the fluid exits. At this boundary, a fully developed flow is assumed, and the pressure is set to $p^*_{out} = 0$. To apply this boundary condition, the stress tensor $\bar{\bar{T}}^*$ is expressed in its expanded form as $\bar{\bar{T}}^* = \frac{2}{\phi^*}\bar{\bar{D}}^* - p^*\bar{\bar{I}}$ in Equation 3-5.

$$\Gamma_2 : \left\{ p^*_{out} = 0; \vec{n} \cdot \left(\nabla^* \cdot \vec{u^*}\right) = 0 \longrightarrow \oint_{\Gamma_2} \left[\vec{n} \cdot \left(\frac{2}{\phi^*}\bar{\bar{D}}^* - \cancelto{0}{p^*\bar{\bar{I}}}\right)\right] \cdot \vec{v^*}\, d\Gamma^* = 0 \right. \tag{3-10}$$

– Wall boundary: The wall boundary is a solid surface along which the fluid flows. Impermeability and no-slip conditions are imposed on this boundary. For a stationary wall, the velocity is set to zero. Similar to the inlet boundary condition, the weighting functions become zero, thereby canceling the term on the wall boundary.

$$\Gamma_3 : \left\{ \vec{u^*}(x) = 0 \longrightarrow \oint_{\Gamma_3} \left(\vec{n} \cdot \bar{\bar{T}}^*\right) \cdot \cancelto{0}{\vec{v^*}}\, d\Gamma^* = 0 \right. \tag{3-11}$$

– The symmetry boundary is defined as a line in two-dimensional flows or a plane in three-dimensional flows where the fluid flow is symmetric. At this boundary, there is no flow across the symmetry line or plane, ensuring that the normal component of the velocity is zero. Additionally, the stress tensor at the symmetry boundary is null, reflecting the absence of shear stress and normal stress across the boundary

$$\Gamma_4 : \left\{ \vec{n} \cdot \vec{u^*} = 0; \vec{t} \cdot \left(\vec{n} \cdot \bar{\bar{T}}^*\right) = 0 \right. \tag{3-12}$$

3.5 Solution Procedure and Implementation

This work employs a general-purpose finite element code developed in *Python* with the *DOLFIN* (*FEniCS*) framework, allowing the same implementation to handle arbitrary geometries by simply modifying the mesh and boundary descriptions. The numerical simulations ran on a computer with an Intel Core i9-7900X CPU (10 physical cores), 128 GB of DDR4 RAM, and a parallel setup exploiting up to 20 processes. The solver uses the MUMPS library for linear systems and applies Newton's Method to handle the nonlinear equations, with an absolute tolerance of 10^{-9} and a relative tolerance of 10^{-10}.

The approach helps highly nonlinear partial differential equations by iterating on specific rheological parameters until convergence is achieved. The solver tests a power-law index, attempts to converge at that setting, then either adjusts it to a more aggressive (lower) or more conservative (higher) level depending on whether the previous attempt succeeded or failed. The fluid's power-law index is reduced step by step until it reaches the target. This stepwise strategy ensures robustness against strong nonlinearities by continually reverting to a known good solution whenever the solver diverges.

4
Three-dimensional flow in slot coating die

This chapter outlines the fundamental aspects of modeling and simulating three-dimensional flow in a slot coating die, with a focus on the behavior of thixotropic fluids. The geometry and rheological data used are based on the work of Meng, Wang e Chen (2011), who conducted experiments and simulations using the power-law model to describe the fluid's rheological response. This setup was later validated by Igali et al. (2020), ensuring the reliability of computational fluid dynamics for this type of application.

The objective of this study is to implement a thixotropic model using the geometry and fluid rheology described by Meng, aiming to analyze the effects of thixotropy on the flow within the coating die. To achieve this, two rheological models are compared: the Generalized Newtonian Model (GNM), where viscosity is solely a function of the shear rate, and the Thixotropy Model, which considers viscosity as dependent not only on the shear rate but also on the fluid's deformation history.

The methodology includes a detailed description of the geometric properties of the die, the rheological parameters of the fluid, and the boundary conditions applied. A mesh convergence analysis is also conducted to ensure the accuracy of the numerical results. This chapter serves as the foundation for the presentation and discussion of the simulation results, which will be detailed in the following chapter, where the effects of thixotropy and their implications for slot die design will be explored.

4.1
Geometry properties

The schematic diagram of a coat-hanger die, shown in Figure 4.1, illustrates the geometric parameters explored in this study. Specifically, $A-A$ represents the symmetry plane cross-section view, R_i is the radius of the die inlet tube, $R(x)$ denotes the radius of the manifold, α is the manifold angle, B represents the land height, L is the half width of the die, and H is the height of the slot.

The geometric parameters of the coat-hanger die are listed in Table 4.1. The manifold radius is determined using Equation 4-1, where x represents the distance from the symmetry plane $A-A$.

$$R(x) = 10(1-(x/2L))\ x \in (0 \sim L) \tag{4-1}$$

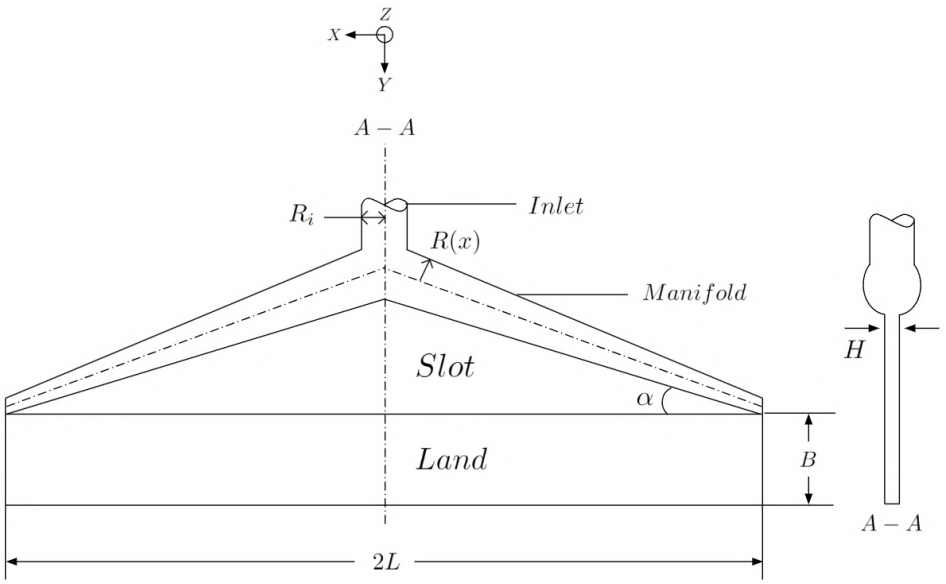

Figure 4.1: Schematic representation of a coat-hanger die. (Adapted from Meng, Wang e Chen (2011))

Table 4.1: Geometric parameters of coat-hanger die.

L (mm)	H (mm)	α (°)	B (mm)	R_i (mm)
168	1.5	30	50	10

4.2 Rheological properties

The analysis considers two different rheological models. The first model, named Time-Independent Model (TIM), simplifies the fluid behavior by ignoring time-dependent effects. It assumes that viscosity at each point is a function of the local deformation rate, $\dot{\gamma}$, without considering any temporal variations.

The rheological parameters K and n employed in this study were the same as those utilized by Meng, Wang e Chen (2011), with values of 0.799 $Pa.s^n$ and 0.696, respectively. Furthermore, the Newtonian plateaus, ϕ_0 and ϕ_∞, were defined based on standard values from battery manufacturing processes, set at 0.02 $Pa^{-1}.s^{-1}$ and 100 $Pa^{-1}.s^{-1}$, respectively.

The primary objective of this study is to analyze the effects of thixotropy on the slot coating process. This analysis will be conducted by evaluating results at two different volumetric flow rates Q and varying values of the thixotropy number (Λ), a dimensionless parameter used to define the characteristic times of thixotropy which is defined as the ratio of the construction or avalanche time to the characteristic liquid residence time Eq. (4-2). This approach aims to provide a comprehensive understanding of how thixotropy influences the velocity profile uniformity at the outlet of the coat-hanger die.

$$\Lambda = \frac{t \cdot Q}{L \cdot \bar{A}} \tag{4-2}$$

where $\bar{A}$ denotes the mean cross-sectional area of the manifold, given by

$$\bar{A} = \frac{1}{L} \int_0^L \pi R(x)^2 \, dx \tag{4-3}$$

4.3 Dimensionless numbers

As outlined in Section 2.3, specific scaling parameters were chosen to perform a dimensionless analysis of mass and momentum conservation equations, and fluidity equations. To solve the slot coating die flow, the maximum velocity from the imposed inlet velocity profile, determined by a given volumetric flow rate, was chosen as the characteristic velocity and the width of the slot gap was used as the characteristic length.

4.4 Boundary conditions

The boundary conditions for the flow within the coat-hanger can be written as follows: A power law velocity profile as described by Chin (2012) and given by Equation 4-4 is imposed at the inlet tube.

$$u(y,z) = \frac{Q}{\pi R^3} \left(\frac{3n+1}{R^{\frac{1}{n}}(n+1)} \left(R^{\frac{n+1}{n}} - \left(\sqrt{(y-y_0)^2 + (z-z_0)^2} \right)^{\frac{n+1}{n}} \right) \right) \tag{4-4}$$

As discussed in the previous section, the maximum velocity from this imposed inlet velocity profile was selected as the characteristic velocity. Consequently, the non-dimensional form of this velocity profile, as defined by Equation 4-5, is applied at the inlet surface.

$$u^*(y,z) = 1 - \left\{ \frac{\left[(y-y_0)^2 + (z-z_0)^2 \right]^{\frac{1}{2}}}{R} \right\}^{\frac{n+1}{n}} \tag{4-5}$$

This velocity profile corresponds to an equilibrium fluidity, denoted as ϕ^*_{eq} (Equation 2-6), which is imposed to maintain consistency in the flow characteristics. At the outflow surface, a pressure value of $p^*_{out} = 0$ is applied. Along the wall surfaces, impermeability and no-slip conditions are imposed, i.e. $\vec{u^*} = 0$.

To save computational time, only one-quarter of the domain geometry is simulated, with symmetry boundary conditions applied to two surfaces. Figure 4.2 provides a depiction of the model geometry and boundary conditions for the flow within the coat-hanger. The figure details the entire system setup, including the specific boundary conditions applied at each surface.

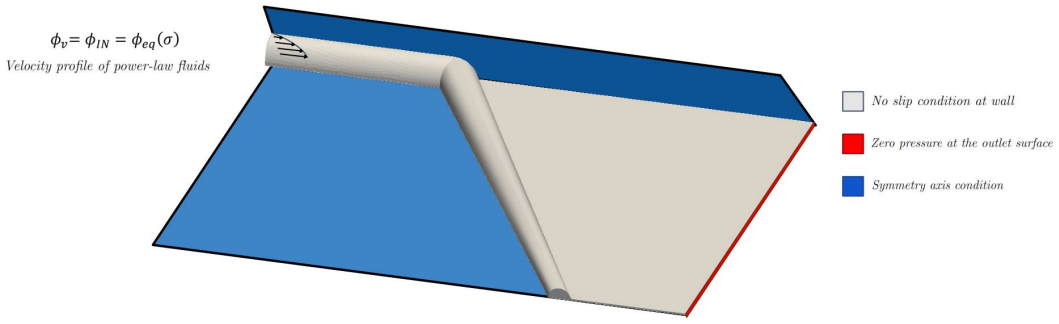

Figure 4.2: Model geometry and boundary conditions for the coat-hanger.

4.5 Solution method

4.5.1 Mesh convergence analysis

In any numerical implementation, the computational domain discretization influences the accuracy and reliability of the results. A well-constructed mesh captures flow features and gradients effectively, whereas an inadequate mesh can lead to numerical inaccuracies or convergence issues.

Mesh convergence analysis is used to validate numerical models and ensure that simulation results are independent of the mesh element size. This method involves systematically refining the mesh and assessing the impact on key variables of interest. The primary goal is to reach a point where further refinement does not produce significant changes in the results, indicating that the solution has become mesh-independent.

The initial step involved generating a coarse mesh to conduct preliminary simulations. This mesh provided a baseline for identifying regions within the computational domain where the mesh needed to be refined.

A mesh refinement strategy was implemented, progressively increasing the mesh density both globally and locally. Global refinement involved increasing the total number of elements throughout the computational domain, while local refinement focused on areas with expected high gradients, such as near walls and slot. Figure 4.3 shows the meshes used in mesh test.

Simulations were performed on each of these meshes using identical solver settings and boundary conditions to ensure consistency. The only difference between the simulations was the density of the mesh. The results from each mesh were compared by analyzing velocity profiles along the outflow plane of the slot, and differences between successive mesh refinements were quantified to assess convergence.

Building upon this approach, the mesh was systematically refined and the

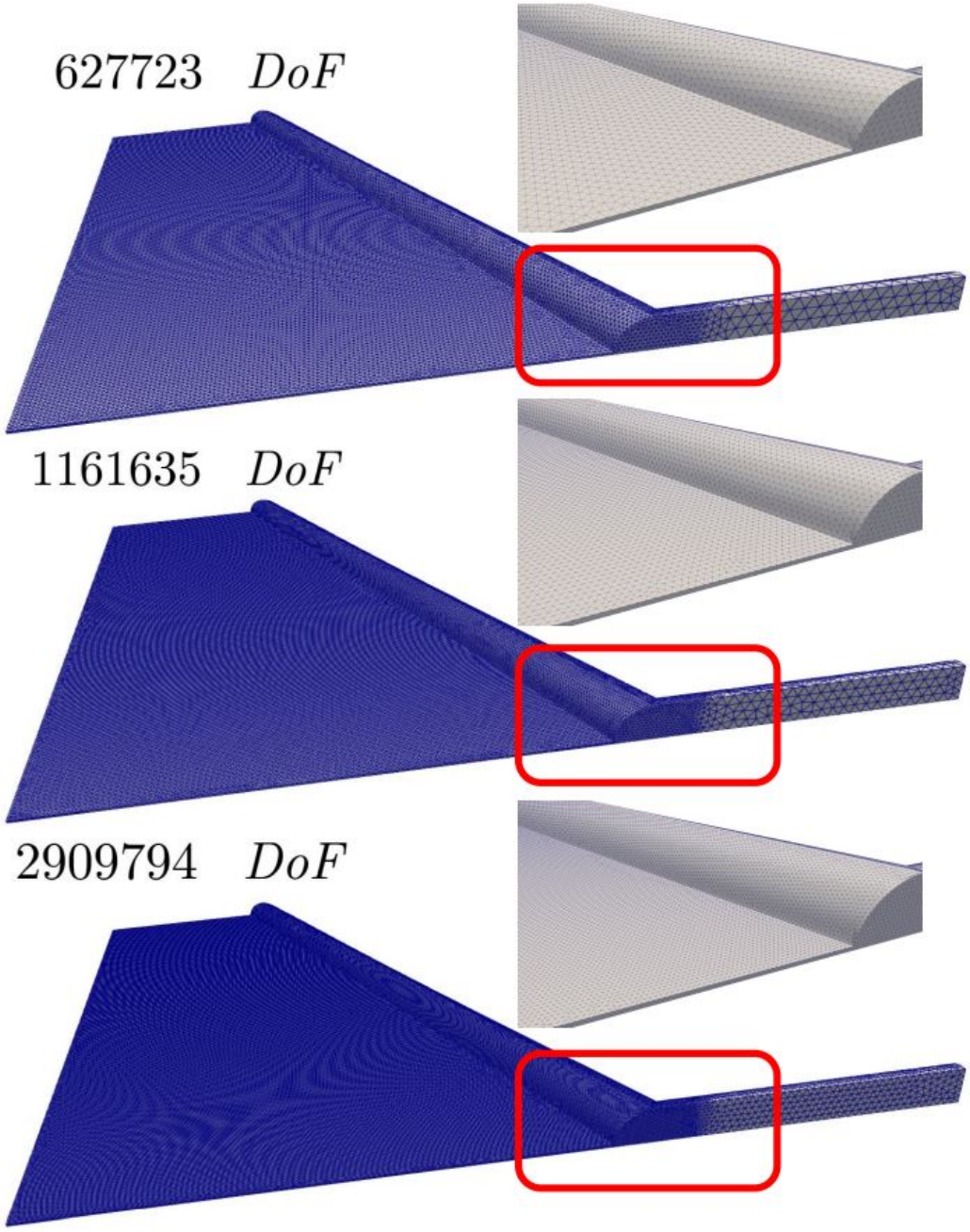

Figure 4.3: Meshes used in convergence analysis.

velocity at the outlet was evaluated using the Mean Absolute Percentage Error (MAPE) as the convergence criterion. When the number of degrees of freedom (DoF) increased from 627.723 to 1.161.635, the MAPE for outlet velocity was 3.46%. Further refinement of the mesh from 1.161.635 DoF to 2.909.794 DoF decreased the MAPE to 1.09%. Among all geometries studied, this particular configuration exhibited the largest MAPE difference, representing the worst-case scenario.

To visualize these differences, Figure 4.4 presents the velocity profile along the outlet for the various mesh resolutions. From this comparison,

the curves for the finest meshes nearly overlap, confirming that additional refinement has a negligible impact on the velocity distribution.

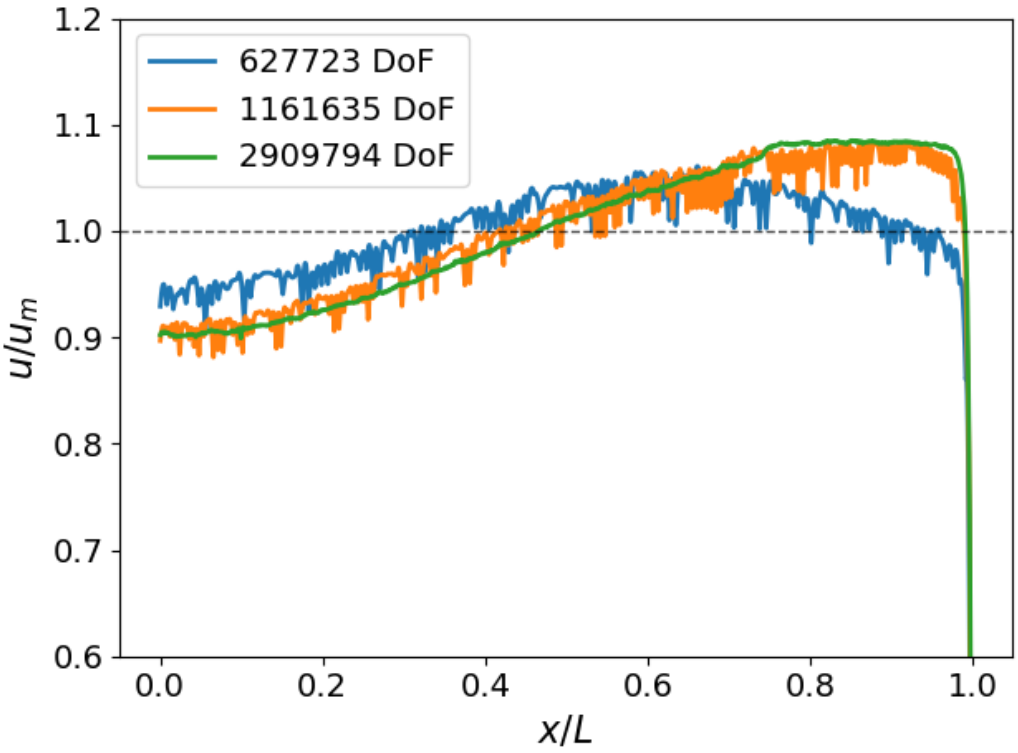

Figure 4.4: Velocity profile across the web direction for various mesh resolutions.

5
Results

The main objective of this study is to analyze the influence of thixotropic behavior on the flow inside coating dies, comparing the results obtained with a viscous thixotropic model (MENDES; ABEDI; THOMPSON, 2018) with those obtained with a GNM, which neglects time-dependent viscosity effects. The comparison focuses on evaluating the influence of the model on flow characteristics such as velocity distribution, pressure fields, and fluidity fields, providing a comprehensive understanding of how time-dependent microstructural rearrangements affect the flow. It is important to note that most of die design procedure used in the industry neglects thixotropic effects. The results presented here will show how accurate this hypothesis is.

Two flow rates are examined $Q = 2.275 \times 10^{-5} m^3/s$ and $Q = 5.685 \times 10^{-4} m^3/s$. Three thixotropic numbers (Λ) are analyzed: $\Lambda = 0.05$, $\Lambda = 1$, and $\Lambda = 5$. For simplicity, the avalanche time is assumed to be equal to the construction time. Therefore, the results discussed in this chapter do not represent the behavior of any specific fluid. The lower thixotropic number serves as a reference for approximating the time-independent scenario. As Λ increases, the fluid's internal structure becomes more resistant to immediate rearrangement, emphasizing the role of time-dependent effects.

The initial simulation results revealed an uneven velocity distribution at the die exit, with higher velocities near the edges compared to the slot center. To address this, geometric modifications were implemented with the goal of achieving a more uniform velocity profile. In industrial applications, it is a common practice to use simulation results to guide a geometry optimization process, in order to obtain better flow rate uniformity. The chapter will also discuss the comparative results between the original and modified geometries, highlighting how the adjustments improved the velocity distribution, bringing it closer to the desired uniformity across the width of the die.

5.1
Velocity Fields

Figures 5.1 and 5.2 presents the velocity magnitude along the symmetry plane at both flow rates and rheological models considered. Regardless of the flow rate, all models exhibit qualitatively similar velocity field throughout the distribution chamber and slot. In general, the velocity is lower at the slot, but at all conditions, there is a region of high velocity near the edge of the slot.

The geometry of the die cavity is such that it leads to a non-uniform flow rate distribution.

The velocity profile along the width of the die is presented in Figures 5.3.a and 5.3.b. The velocity u is normalized with respect to the average velocity u_m and the width is normalized with respect to L. The dimensionless results indicate no significant change in the curves shapes for the different tested flow rates. For the lower thixotropic number, the exit velocity profile closely resembles of the GNM, as expected. As thixotropic number increases, the fluid's microstructure responds more slowly, manifesting as localized variations in the velocity at the exit.

For this particular geometry, the velocity tends to be higher at the ends of the slot compared to the middle, regardless of the thixotropic parameter. This makes the geometry undesirable for practical applications, as it fails to produce a uniform velocity profile. Therefore, further modifications are necessary to achieve a more even velocity distribution across the slot, ensuring a consistent coating layer.

One key conclusion from these results is that the time-dependent nature of viscosity has a significant impact on the flow, especially in geometries where the velocity profile must be carefully controlled to avoid defects in the final product. In the context of slot coating, neglecting thixotropic effects can lead to inaccurate flow predictions and consequently non-optimal die design

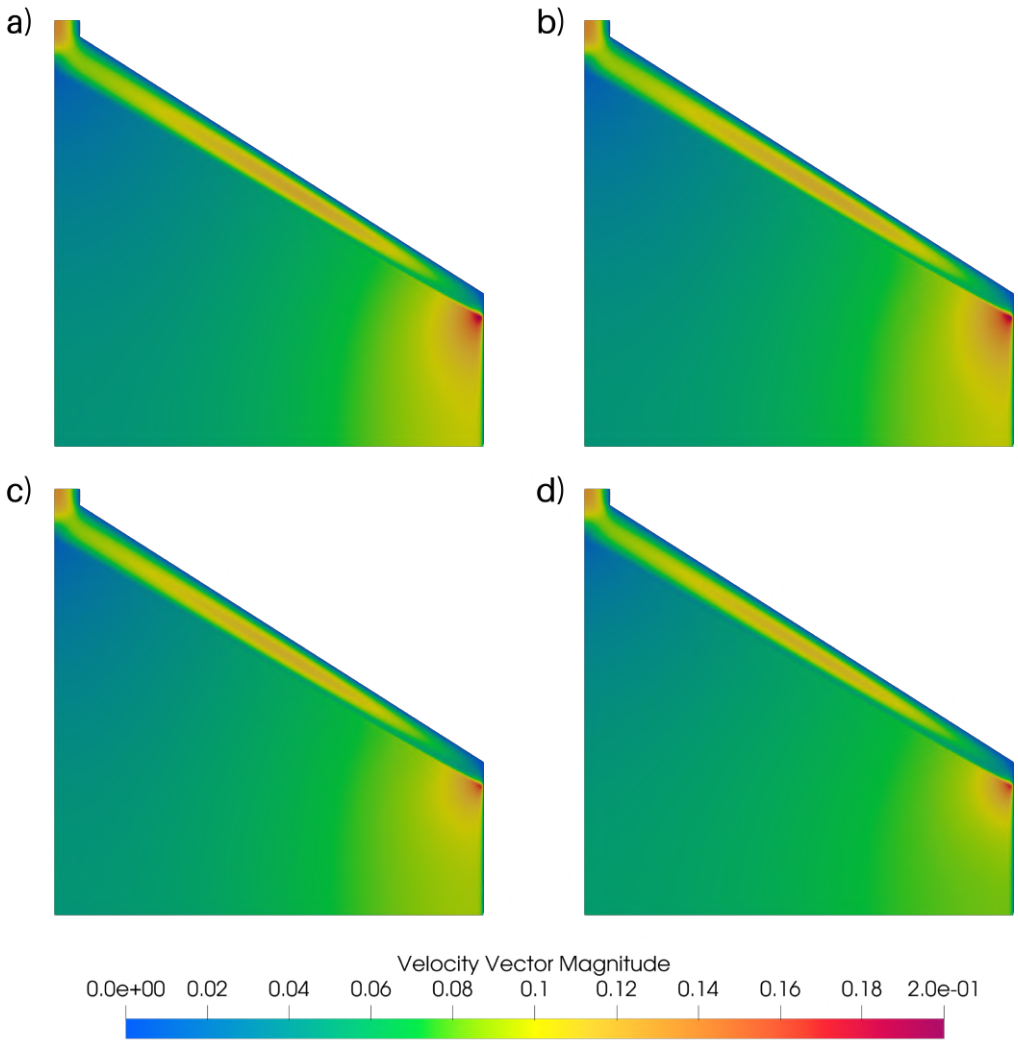

Figure 5.1: Velocity field at the central plane of the coat-hanger with $Q = 2.275 \times 10^{-5}\ m^3.s^{-1}$: (a) time-independent model, (b) time-dependent model $\Lambda = 5 \times 10^{-2}$, (c) time-dependent model $\Lambda = 1$, (d) time-dependent model $\Lambda = 5$.

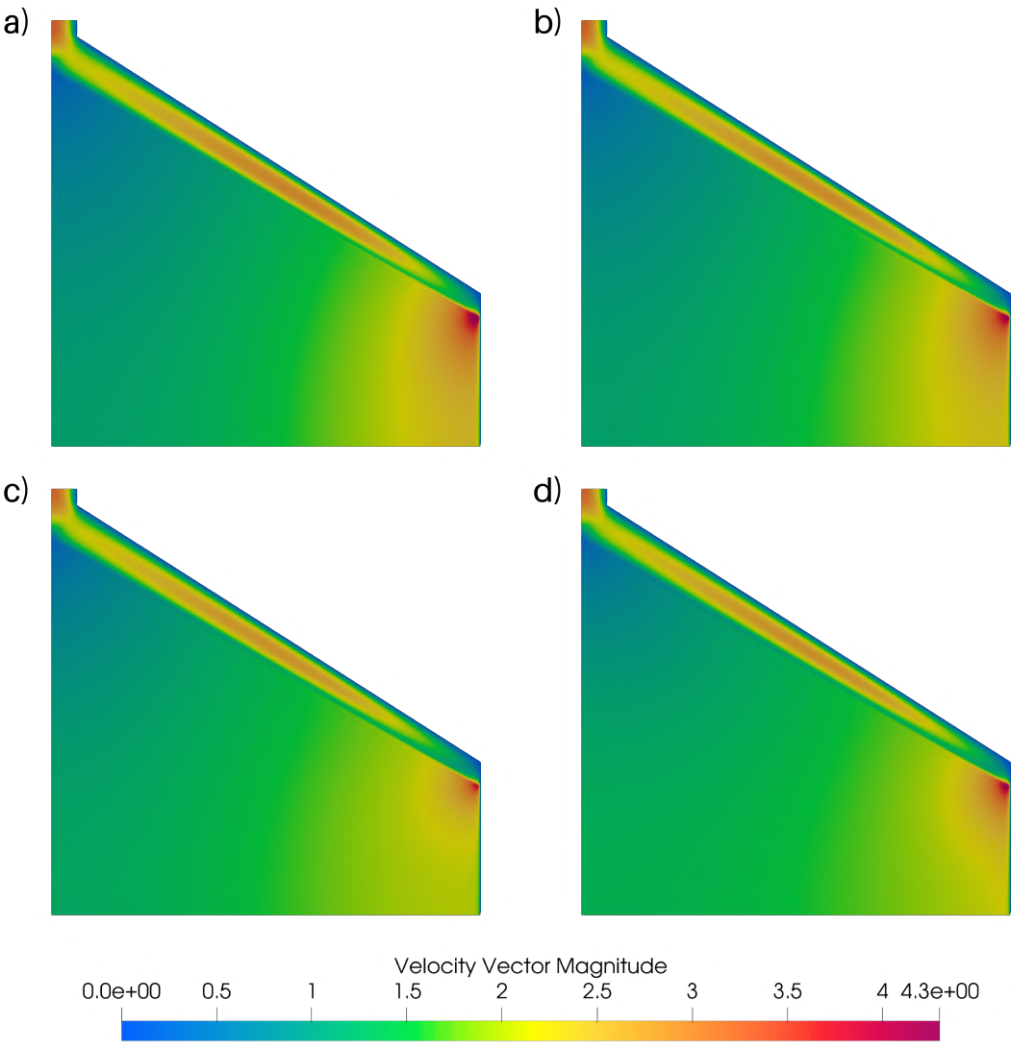

Figure 5.2: Velocity field at the central plane of the coat-hanger with $Q = 5.685 \times 10^{-4}\ m^3.s^{-1}$: (a) time-independent model, (b) time-dependent model $\Lambda = 5 \times 10^{-2}$, (c) time-dependent model $\Lambda = 1$, (d) time-dependent model $\Lambda = 5$.

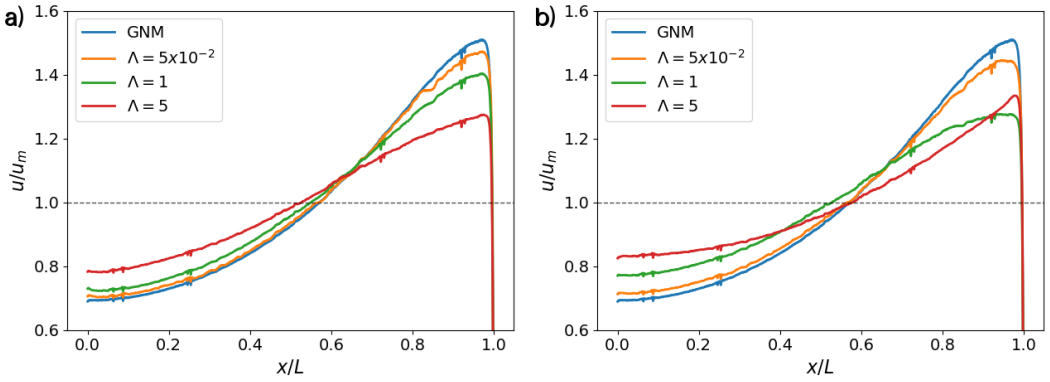

Figure 5.3: Velocity distribution over the width for the Generalized Newtonian model and thixotropic model at different values Λ: (a) $Q = 2.275e^{-5}\ m^3.s^{-1}$, (b) $Q = 5.685e^{-4}\ m^3.s^{-1}$.

5.2 Pressure Fields

Figures 5.4 and 5.5 show pressure fields along the symmetry plane at both flow rates and provide information on how thixotropic behavior influences the pressure distribution inside the coating die. As expected, the pressure is higher along the distribution chamber. Moreover, because of the weaker flow resistance, the pressure gradient along the distribution chamber is much lower than that along the slot.

As thixotropic number increases, the pressure in the distribution chamber rises. This effect is evident at both flow rates. The stress rises as the liquid moves from the distribution chamber to the slot. For the time-independent model, the liquid viscosity quickly drops to the value associated with the higher stress. For the thixotropic model, the viscosity does not drops as fast as the liquid moves to the slot, leading to higher viscosity and consequently higher pressure. This may cause the equipment to be under-designed for the mechanical stresses encountered, leading to premature mechanical failures. This effect is stronger in the higher flow rate case.

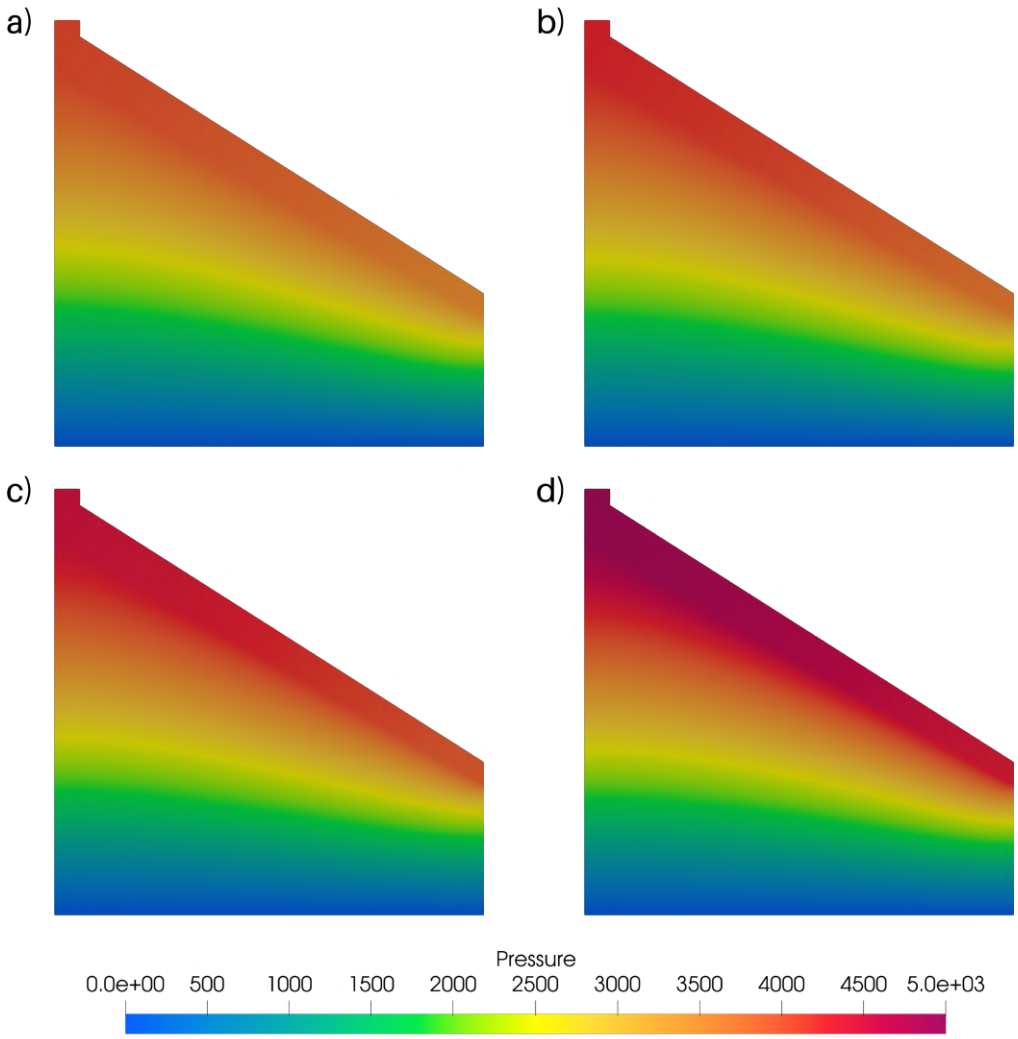

Figure 5.4: Pressure field at the central plane of the coat-hanger with $Q = 2.275 \times 10^{-5}\ m^3.s^{-1}$: (a) time-independent model, (b) time-dependent model $\Lambda = 5 \times 10^{-2}$, (c) time-dependent model $\Lambda = 1$, (d) time-dependent model $\Lambda = 5$.

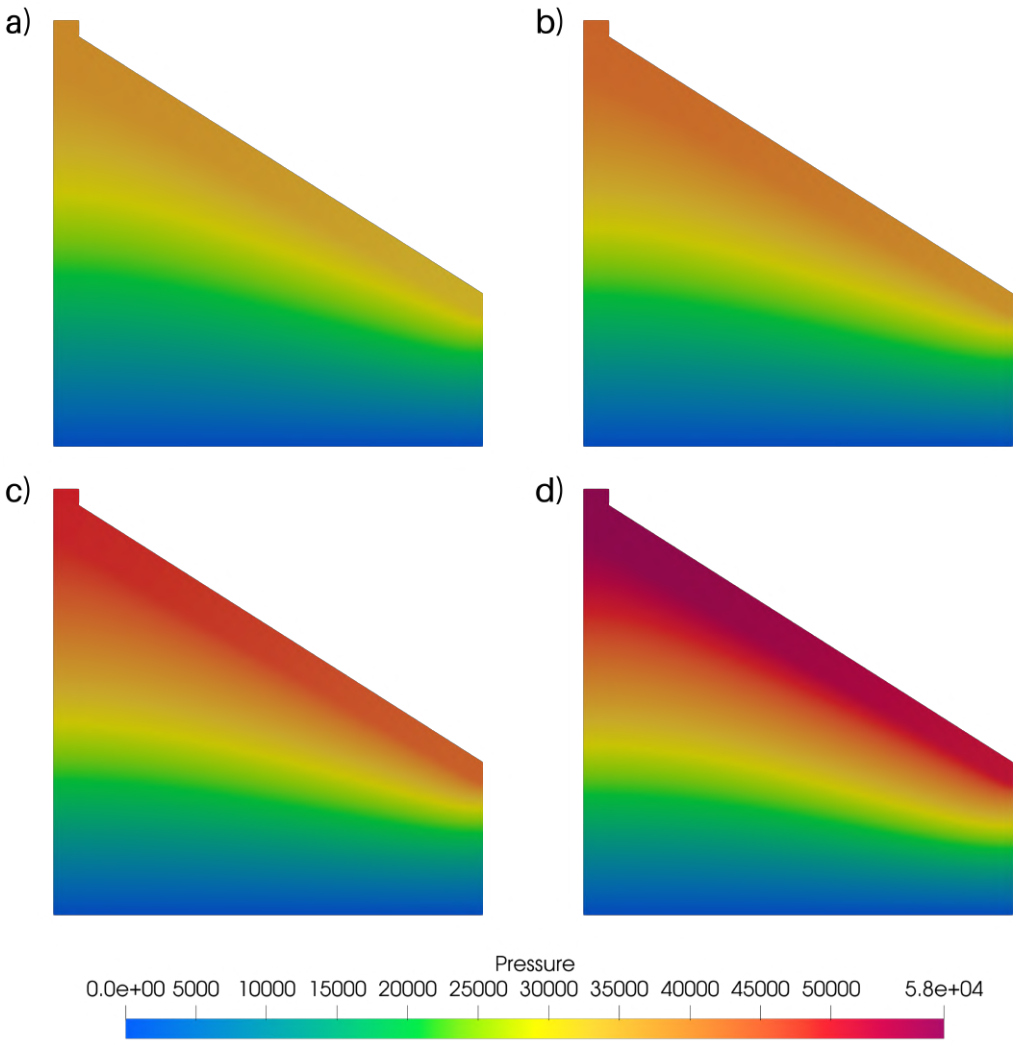

Figure 5.5: Pressure field at the central plane of the coat-hanger with $Q = 5.685 \times 10^{-4}\ m^3.s^{-1}$: (a) time-independent model, (b) time-dependent model $\Lambda = 5 \times 10^{-2}$, (c) time-dependent model $\Lambda = 1$, (d) time-dependent model $\Lambda = 5$.

5.3 Fluidity Fields

Figures 5.6 and 5.7 results the fluidity fields along the wall for both rheological models and both flow rates. In the GNM scenario, there is a sudden increase in fluidity when the fluid enters the slot and undergoes a high shear rate due to the narrowing of the geometry, as the model assumes that the viscosity responds instantly to changes in shear conditions.

However, as thixotropic number increases, the fluidity becomes more affected by its deformation history over time. In this case, when the fluid leaves the distribution chamber and enters the slot, the fluidity does not respond instantaneously to changes in stress. Instead, the microstructure takes time to adjust, which smooths out the transition between low and high fluidity

regions. This results in a more gradual and continuous fluidity profile, without the abrupt increases seen in the time-independent model. The lower fluidity in the slot observed with the thixotropic model leads to higher pressure in the distribution chamber discussed before.

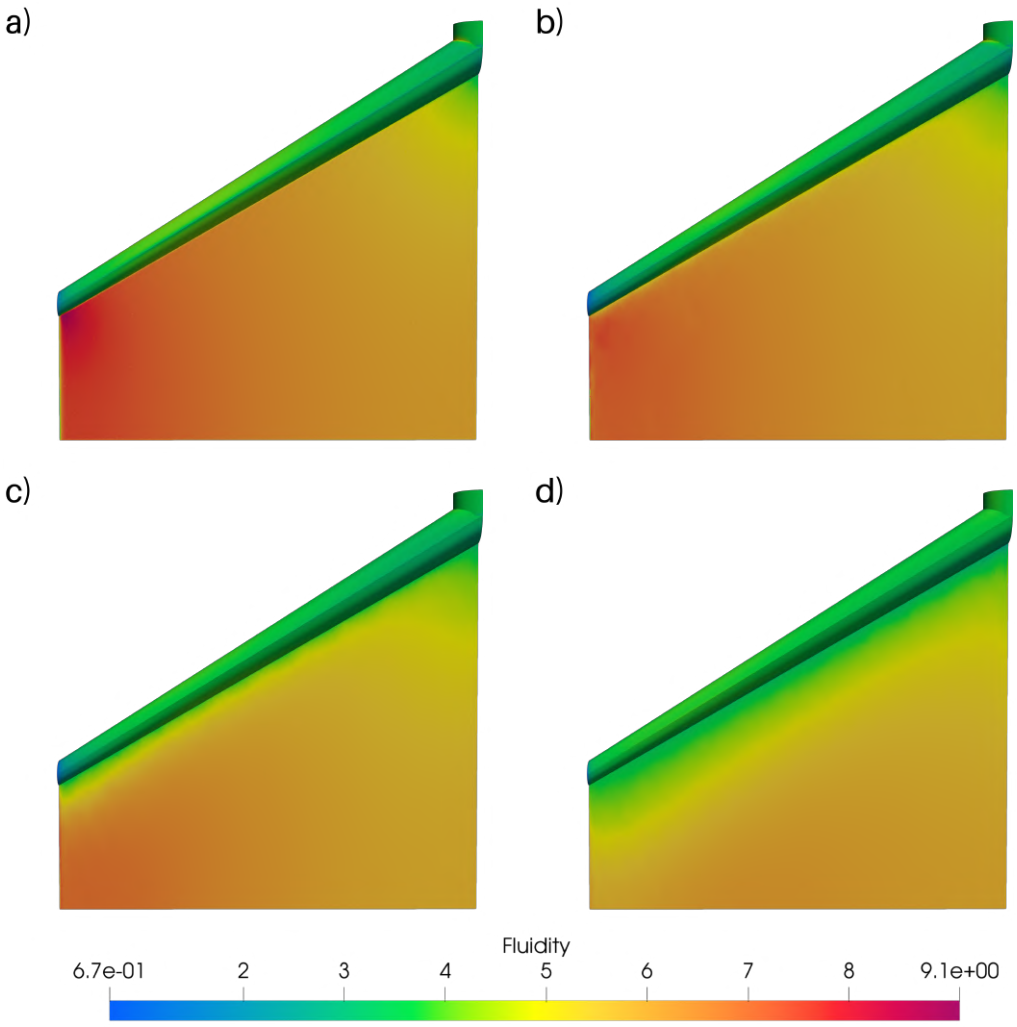

Figure 5.6: Fluidity field at the wall of the coat-hanger with $Q = 2.275 \times 10^{-5}\ m^3.s^{-1}$: (a) time-independent model, (b) time-dependent model $\Lambda = 5 \times 10^{-2}$, (c) time-dependent model $\Lambda = 1$, (d) time-dependent model $\Lambda = 5$.

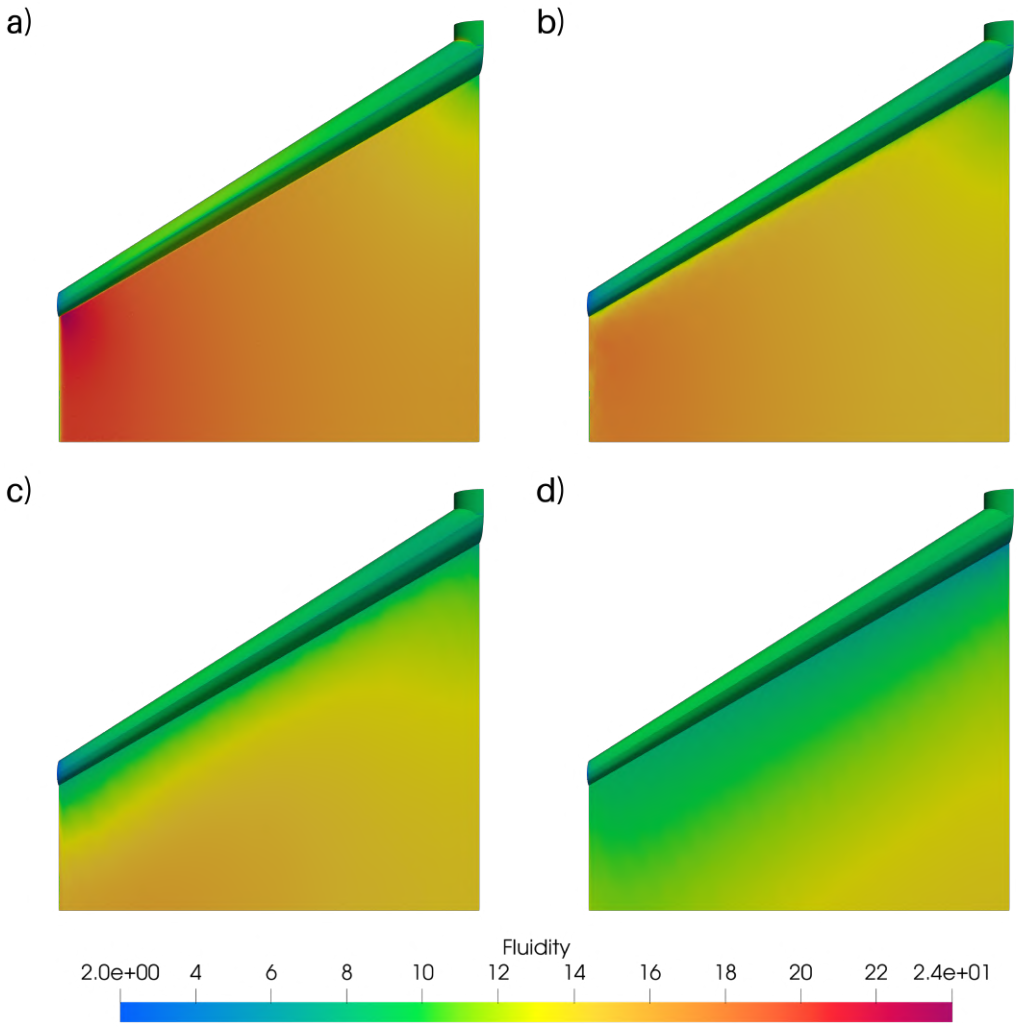

Figure 5.7: Fluidity field at the wall of the coat-hanger with $Q = 5.685 \times 10^{-4}\ m^3.s^{-1}$: (a) time-independent model, (b) time-dependent model $\Lambda = 5 \times 10^{-2}$, (c) time-dependent model $\Lambda = 1$, (d) time-dependent model $\Lambda = 5$.

5.4 Modifications to the original geometry

In order to reduce the flow rate non-uniformity profile along the exit of the slot observed, modifications were made to the design of the manifold. Specifically, both the manifold radius and the manifold angle were adjusted. These changes aimed to increase the resistance to fluid flow, thereby minimizing the fluid's tendency to preferentially flow toward the ends of the slot. The aim of these modifications was to achieve a more uniform velocity profile across the web direction.

Previous research, such as that conducted by Wang, Chen e Huang (2006), has investigated the effects of the distributor's geometric parameters on the uniformity of transverse flow distribution. These insights informed the

design adjustments made in this study, with the intent of improving flow uniformity and performance during the coating process.

By implementing these changes, the goal was to ensure a more uniform and efficient coating application, effectively overcoming the limitations of the original geometry.

The radius of the manifold ($R(x)$) was adjusted, and the new radius is now determined using Equation 5-1, which further helps to regulate the flow distribution across the slot width. For the manifold angle (α), two modified designs were proposed, First modification reduces the manifold angle from 30 degrees to 10 degrees as shown in Table 5.1 and Second modification uses 5 degrees instead (Table 5.2). These changes were intended to shorten the fluid's path in the middle of the slot and reduce the difference in flow resistance between the slot's center and its ends.

Table 5.1: Geometric parameters of First modification coat-hanger die.

L (mm)	H (mm)	α (°)	B (mm)	R_i (mm)
168	1.5	10	50	10

Table 5.2: Geometric parameters of Second modification coat-hanger die.

L (mm)	H (mm)	α (°)	B (mm)	R_i (mm)
168	1.5	5	50	10

$$R(x) = 10(1 - (4x/5L)) \; x \in (0 \sim L) \tag{5-1}$$

A comparison of the exit velocity profile predicted by the Generalized Newtonian Model (GNM) for the original geometry and the two modifications reveals how effectively the new designs address uniformity. Figure 5.8 presents the dimensionless exit velocity u/u_m plotted against the slot width normalized by L. The original design exhibits an increase near the edges, confirming the tendency of fluid to accelerate toward the slot extremities. In both modified geometries, the curves are substantially flatter, indicating an improved flow distribution. First modification shows the most pronounced improvement, whereas Second modification, with its slightly smaller angle, achieves even more reduction in edge velocity.

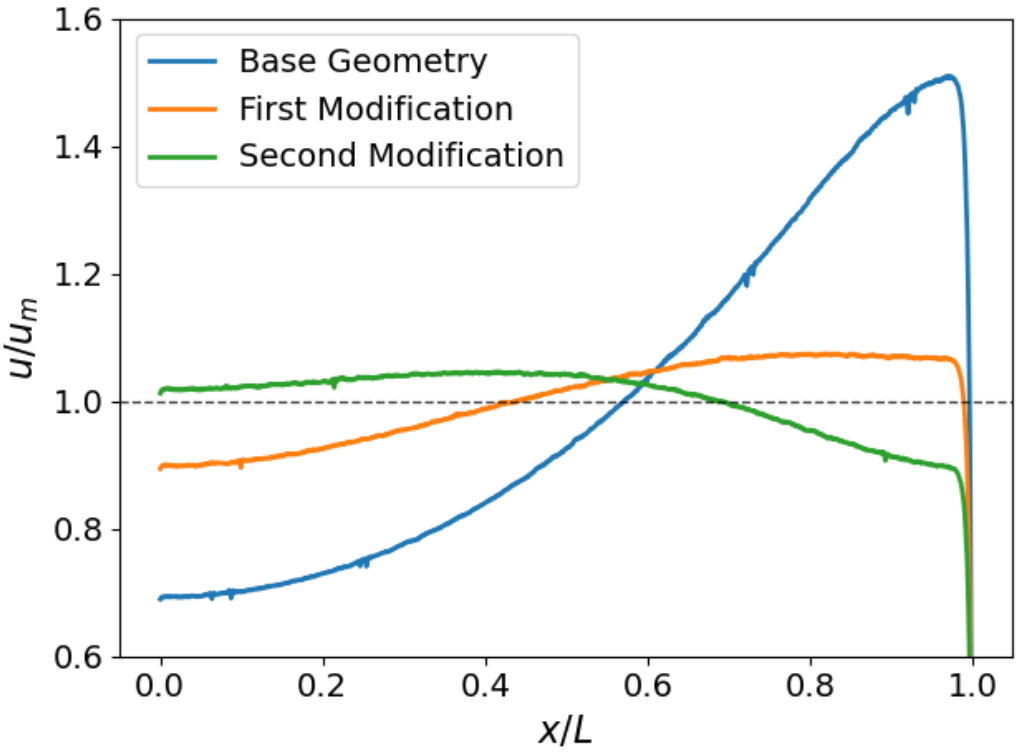

Figure 5.8: Comparison of exit velocity profiles for the Generalized Newtonian Model across three geometries: the original design, First modification ($\alpha = 10°$), and Second modification ($\alpha = 5°$).

Although the primary objective of the design changes was to improve velocity uniformity, the modifications also affect others flow characteristics, including pressure and fluidity distributions. The following subsections present representative fields for both modified geometries, similar to those shown for the original geometry. For consistency, each set of figures corresponds to simulations performed at the same flow rates and model parameters used previously.

5.4.1 Velocity Fields

Figures 5.9 and 5.10 present the exit velocity distributions for the First ($\alpha = 10°$) and Second ($\alpha = 5°$) modifications, respectively, at two different flow rates. Each figure compare the dimensionless velocity profile u/u_m across the slot width (x/L) for the Generalized Newtonian Model (GNM) and three thixotropic cases, $\Lambda = 5 \times 10^{-2}$, $\Lambda = 1$, and $\Lambda = 5$.

Figure 5.9 shows the results for the First geometry modification, where the manifold angle is reduced from 30° to 10°. Unlike the original geometry, this design does not benefit from a stronger thixotropic response. As Λ increases

from 5×10^{-2} to 5, this particular manifold configuration slightly worsens the exit velocity uniformity, which contrasts with the behavior observed in the original geometry. The GNM curve remains closer to a uniform profile, while the $\Lambda = 5$ profile reveals a pronounced rise toward the edge.

In contrast, Figure 5.10 shows the Second geometry modification, where the manifold angle is reduced to 5°. In this geometry, increased thixotropy tends to improve velocity uniformity rather than diminish it. This enhanced uniformity is evident at the lower flow rate (Figure 5.10.a), where the fluid has sufficient time to adjust throughout the slot, resulting in flatter profiles. At the higher flow rate (Figure 5.10.b), the velocity profile becomes uniform as Λ rises from 5×10^{-2} to 1. However, at $\Lambda = 5$, the fluid's microstructure does not have enough time to fully reorganize within the slot, causing a velocity dip in the center and a increase near the edge. This indicates that although lower thixotropic numbers can improve a more uniform flow, higher thixotropic numbers can lead to a different behavior.

These results demonstrate the importance of taking into account time-dependent behavior when designing and optimizing slot coating dies, particularly for thixotropic fluids. While time-dependency is often overlooked in favor of simplified models, this analysis shows that assessing the fluid's response time is crucial to obtain an accurate prediction. Neglecting these effects can lead to suboptimal slot geometry, which may result in defects during the coating process. Therefore, incorporating thixotropic effects into simulations is necessary to ensure the reliability and efficiency of the slot coating die design.

Figures 5.13 through 5.14 show the velocity magnitude fields along the symmetry plane for each modified geometry under varying flow rates and thixotropic parameters. These velocity fields help visualize how the reduced manifold angle alters the fluid's path, shifting flow more toward the slot's midsection and lessening the velocity pattern at the edge seen in the original design. Although specific differences between GNM and higher Λ values have already been detailed, these figures provide an over view of the fluid's velocity distribution in both the first modification and the second modification.

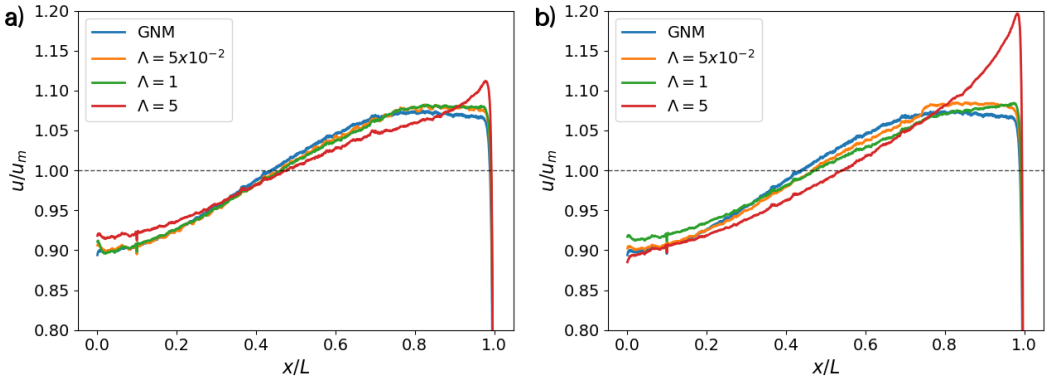

Figure 5.9: Velocity distribution over the width of the First modification coat-hanger for the Generalized Newtonian model and thixotropic model at different values Λ: (a) $Q = 2.275e^{-5}\ m^3.s^{-1}$, (b) $Q = 5.685e^{-4}\ m^3.s^{-1}$.

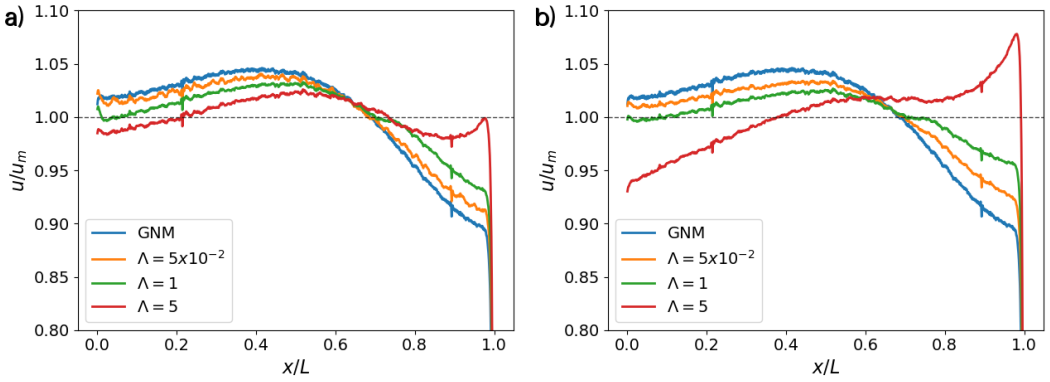

Figure 5.10: Velocity distribution over the width for the Generalized Newtonian model and thixotropic model at different values Λ: (a) $Q = 2.275e^{-5}\ m^3.s^{-1}$, (b) $Q = 5.685e^{-4}\ m^3.s^{-1}$.

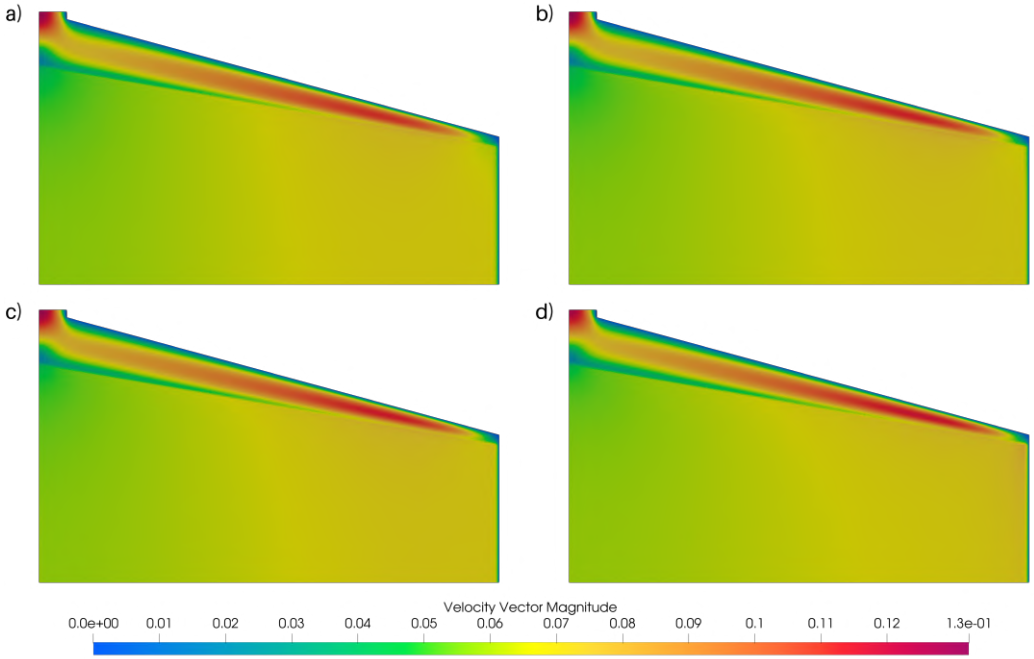

Figure 5.11: Velocity field at the central plane of the First modification coat-hanger with $Q = 2.275 \times 10^{-5}\ m^3.s^{-1}$: (a) time-independent model, (b) time-dependent model $\Lambda = 5 \times 10^{-2}$, (c) time-dependent model $\Lambda = 1$, (d) time-dependent model $\Lambda = 5$.

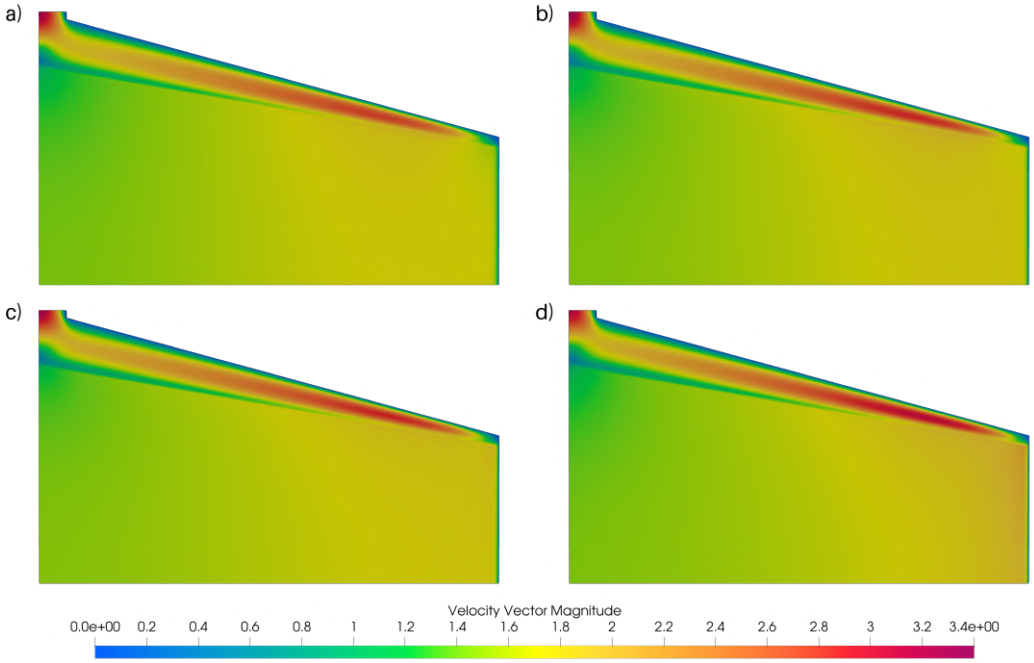

Figure 5.12: Velocity field at the central plane of the First modification coat-hanger with $Q = 5.685 \times 10^{-4}\ m^3.s^{-1}$: (a) time-independent model, (b) time-dependent model $\Lambda = 5 \times 10^{-2}$, (c) time-dependent model $\Lambda = 1$, (d) time-dependent model $\Lambda = 5$.

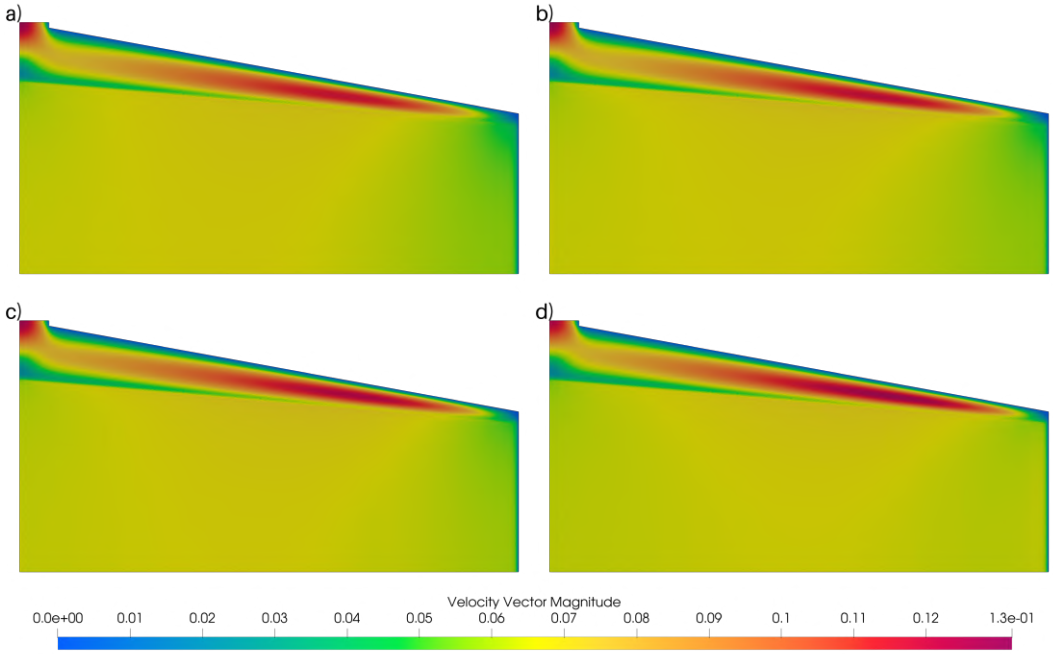

Figure 5.13: Velocity field at the central plane of the Second modification coat-hanger with $Q = 2.275 \times 10^{-5}\ m^3.s^{-1}$: (a) time-independent model, (b) time-dependent model $\Lambda = 5 \times 10^{-2}$, (c) time-dependent model $\Lambda = 1$, (d) time-dependent model $\Lambda = 5$.

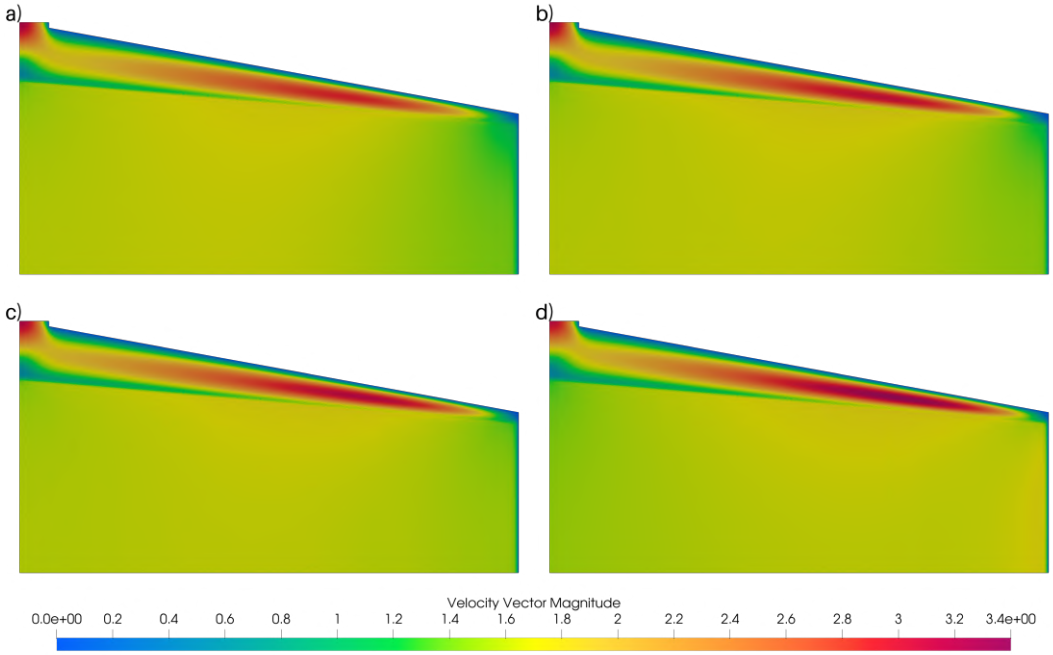

Figure 5.14: Velocity field at the central plane of the Second modification coat-hanger with $Q = 5.685 \times 10^{-4}\ m^3.s^{-1}$: (a) time-independent model, (b) time-dependent model $\Lambda = 5 \times 10^{-2}$, (c) time-dependent model $\Lambda = 1$, (d) time-dependent model $\Lambda = 5$.

5.4.2 Pressure Fields

Figures 5.15 through 5.18 show the pressure fields along the symmetry for First and Second geometry modifications at both flow rates and rheological models, and the general behavior is similar to what has been discussed in the original geometry.

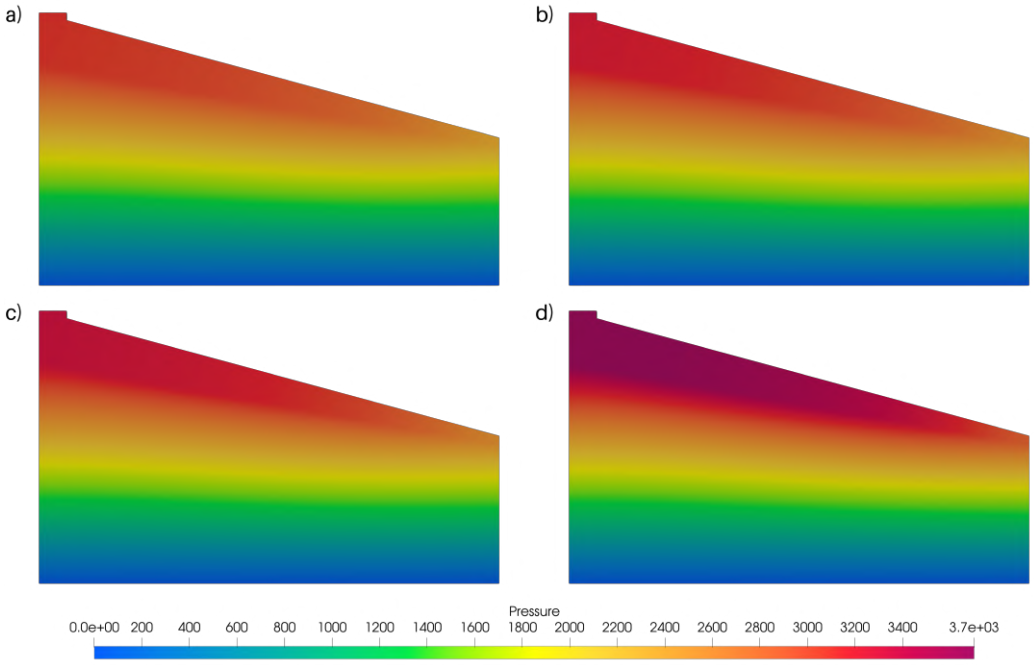

Figure 5.15: Pressure field at the central plane of the First modification coat-hanger with $Q = 2.275 \times 10^{-5}\ m^3.s^{-1}$: (a) time-independent model, (b) time-dependent model $\Lambda = 5 \times 10^{-2}$, (c) time-dependent model $\Lambda = 1$, (d) time-dependent model $\Lambda = 5$.

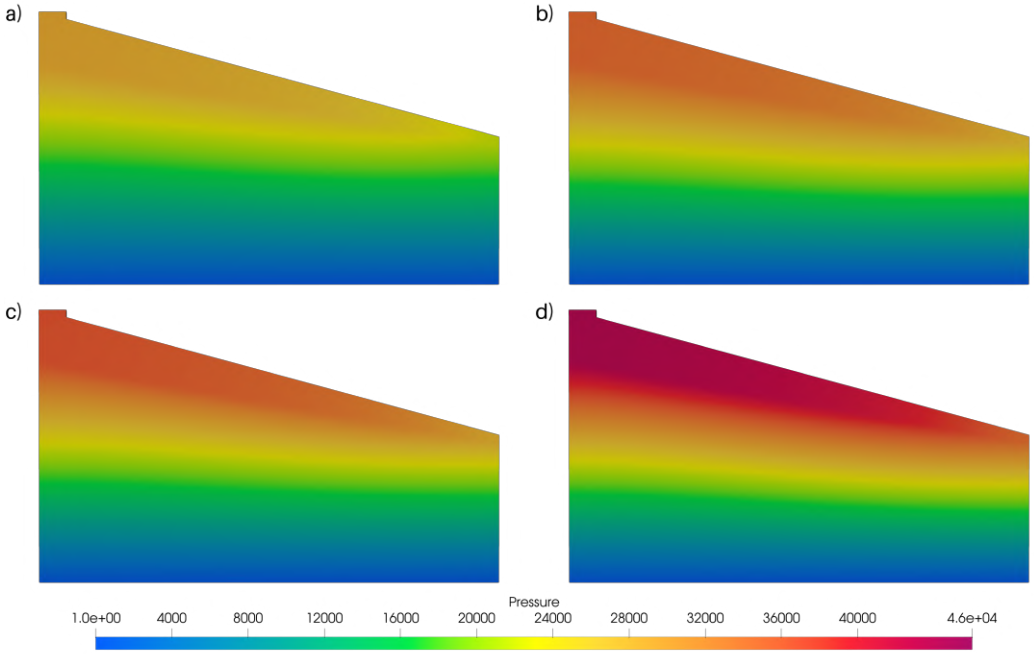

Figure 5.16: Pressure field at the central plane of the First modification coat-hanger with $Q = 5.685 \times 10^{-4}\ m^3.s^{-1}$: (a) time-independent model, (b) time-dependent model $\Lambda = 5 \times 10^{-2}$, (c) time-dependent model $\Lambda = 1$, (d) time-dependent model $\Lambda = 5$.

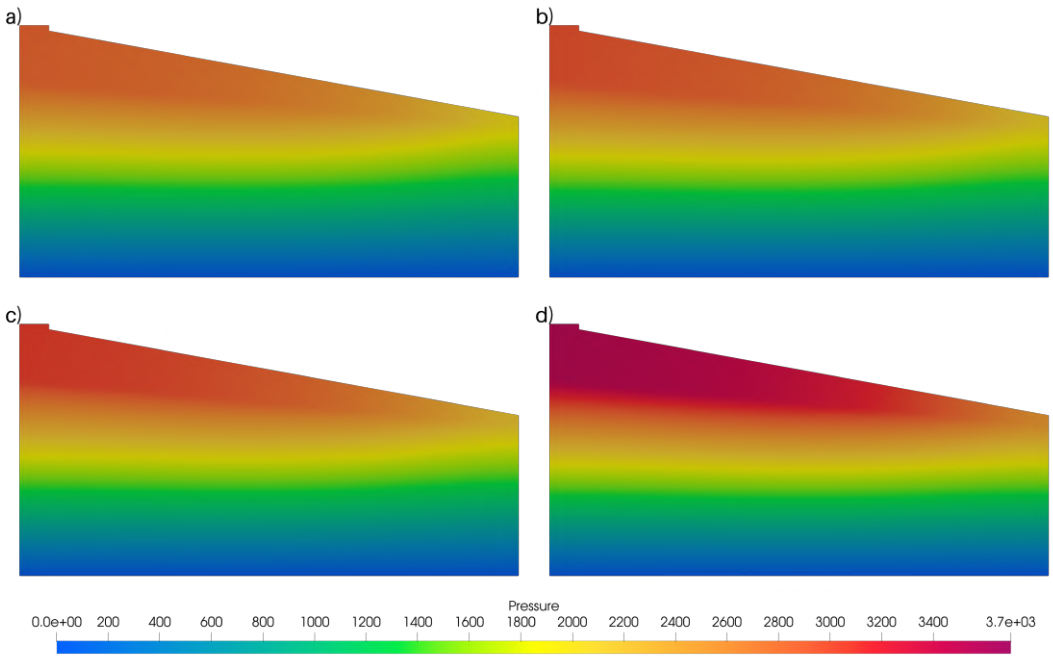

Figure 5.17: Pressure field at the central plane of the Second modification coat-hanger with $Q = 2.275 \times 10^{-5}\ m^3.s^{-1}$: (a) time-independent model, (b) time-dependent model $\Lambda = 5 \times 10^{-2}$, (c) time-dependent model $\Lambda = 1$, (d) time-dependent model $\Lambda = 5$.

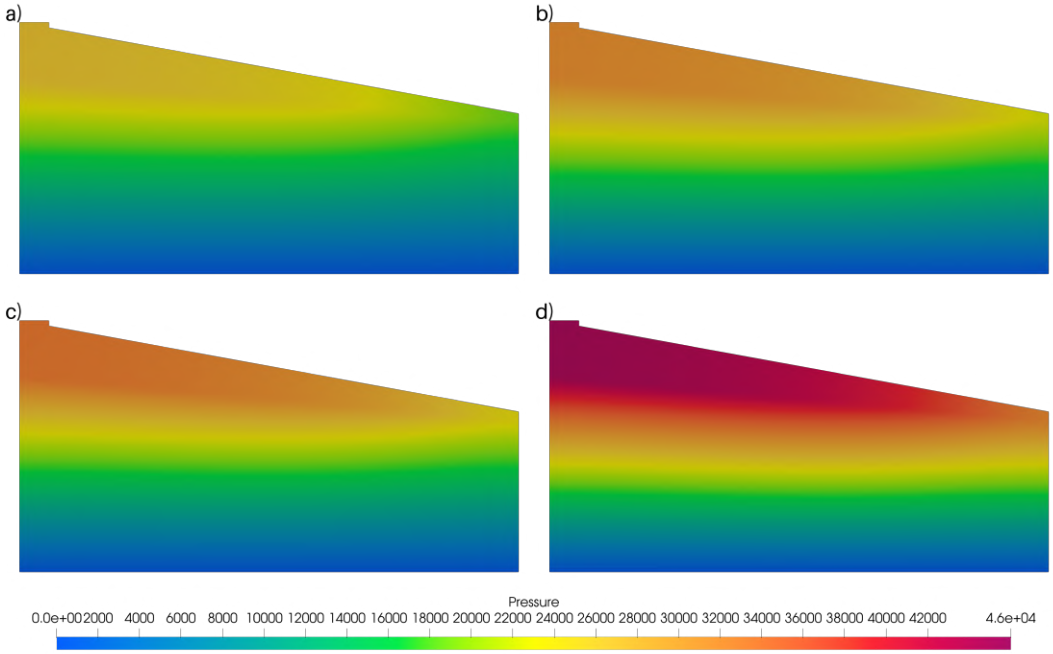

Figure 5.18: Pressure field at the central plane of the Second modification coat-hanger with $Q = 5.685 \times 10^{-4}\ m^3.s^{-1}$: (a) time-independent model, (b) time-dependent model $\Lambda = 5 \times 10^{-2}$, (c) time-dependent model $\Lambda = 1$, (d) time-dependent model $\Lambda = 5$.

5.4.3 Fluidity Fields

Finally, Figures 5.19 through 5.22 show the fluidity fields.

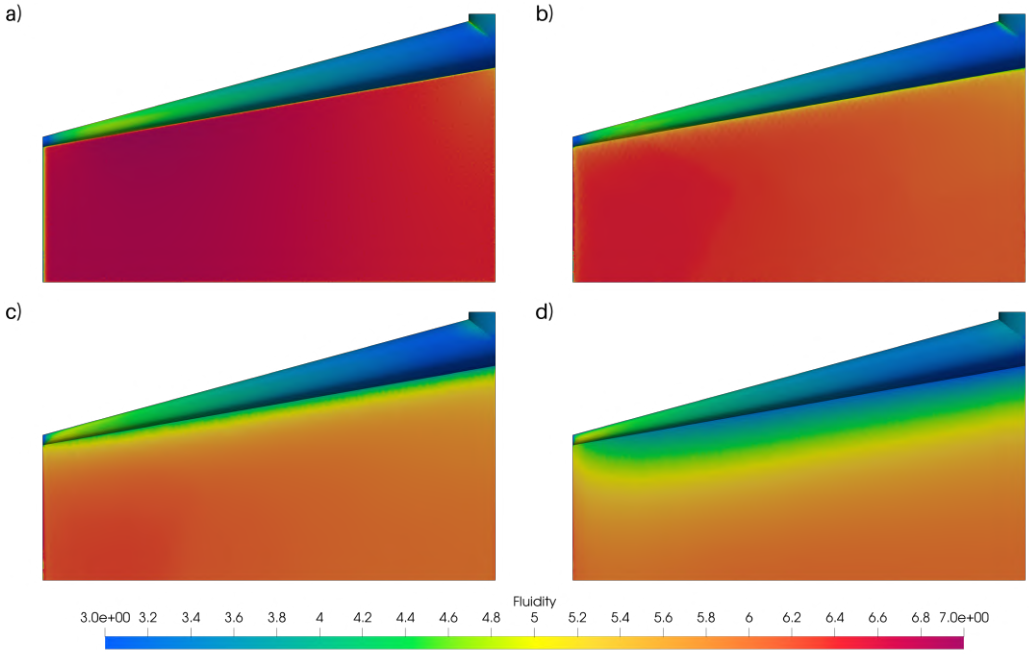

Figure 5.19: Fluidity field at the wall of the First modification coat-hanger with $Q = 2.275 \times 10^{-5}\ m^3.s^{-1}$: (a) time-independent model, (b) time-dependent model $\Lambda = 5 \times 10^{-2}$, (c) time-dependent model $\Lambda = 1$, (d) time-dependent model $\Lambda = 5$.

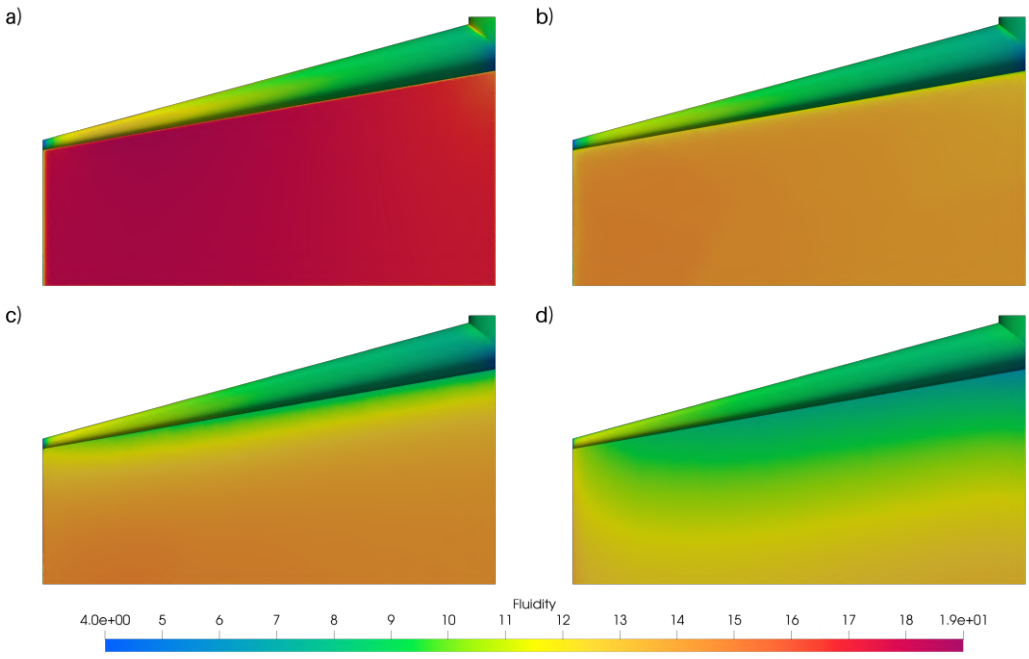

Figure 5.20: Fluidity field at the wall of the First modification coat-hanger with $Q = 5.685 \times 10^{-4}\ m^3.s^{-1}$: (a) time-independent model, (b) time-dependent model $\Lambda = 5 \times 10^{-2}$, (c) time-dependent model $\Lambda = 1$, (d) time-dependent model $\Lambda = 5$.

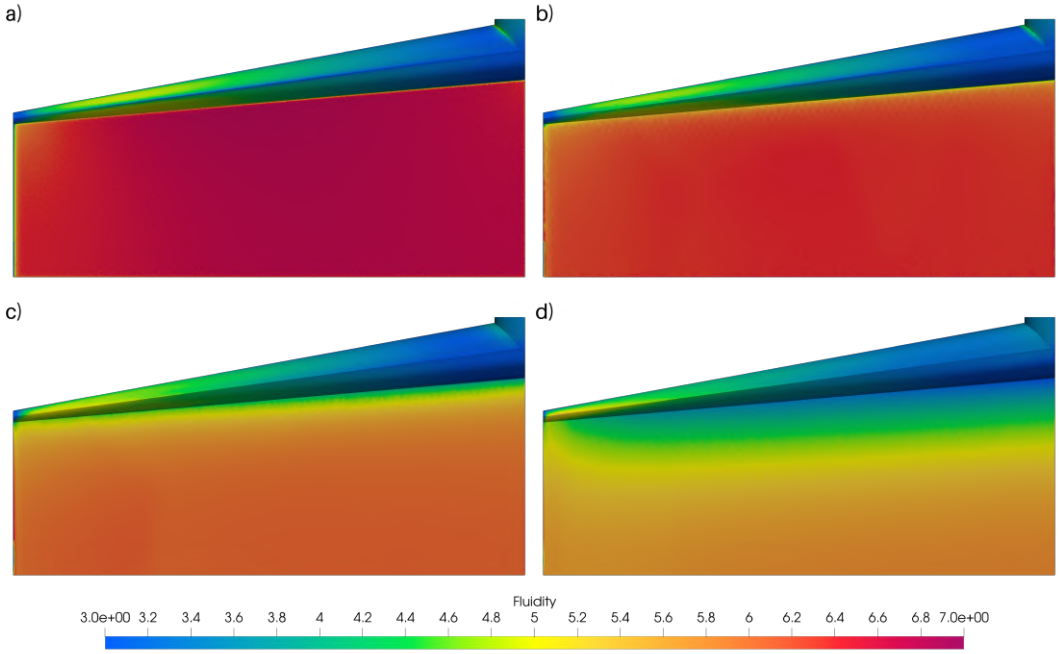

Figure 5.21: Fluidity field at the wall of the Second modification coat-hanger with $Q = 2.275 \times 10^{-5}\ m^3.s^{-1}$: (a) time-independent model, (b) time-dependent model $\Lambda = 5 \times 10^{-2}$, (c) time-dependent model $\Lambda = 1$, (d) time-dependent model $\Lambda = 5$.

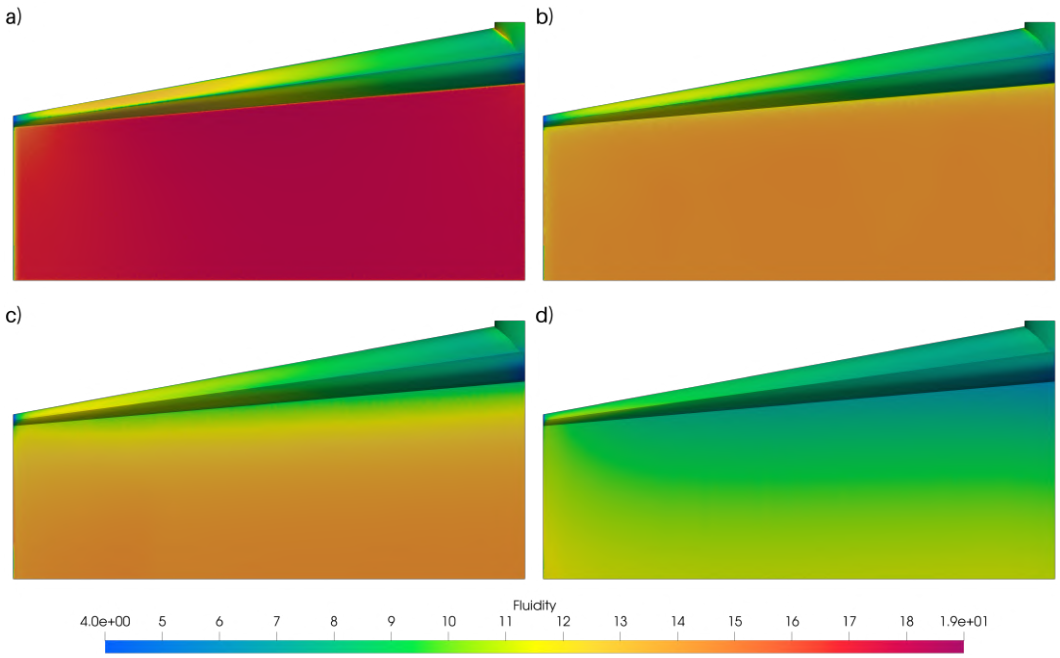

Figure 5.22: Fluidity field at the wall of the Second modification coat-hanger with $Q = 5.685 \times 10^{-4}\ m^3.s^{-1}$: (a) time-independent model, (b) time-dependent model $\Lambda = 5 \times 10^{-2}$, (c) time-dependent model $\Lambda = 1$, (d) time-dependent model $\Lambda = 5$.

6
Conclusions

The effect of thixotropy on the flow inside coating dies was evaluated by comparing the predictions of the three-dimensional flow obtained with two rheological models, one that neglects time-dependent behavior and another that takes that into account. Both models considered have the same viscosity as a function of shear rate.

Only lower thixotropic numbers lead to velocity distribution patterns approaching those obtained with time-independent model, as expected. At higher thixotropic values, it is possible to observe that despite time-dependent behavior of fluids is often neglected, it plays an important role to slot coating head design. Assessment of the fluid's time-dependent characteristics is essential in simulations that aim to accurately predict the flow rate profile at the exit of the coating die. Neglecting this behavior for some fluids, may lead to non-optimal slot geometry determination, which could lead to high film thickness variation in the cross web direction.

Simulations were conducted for three different geometries under identical boundary conditions and rheological properties of the liquid. The original geometry considered was the one used by Meng, Wang e Chen (2011).The first modification involved reducing the manifold angle (α) from 30 degrees to 10 degrees and reducing the manifold radius. These changes were made to increase the resistance to fluid flow through the manifold and in the middle of the slot, aiming to reduce the tendency of the fluid to flow toward the end of the slot and to achieve a more uniform velocity profile across the web direction. The second modification used the same radius adjustment but set the manifold angle to 5 degrees.

For both modified geometries, the results confirmed that the uniform velocity distribution across the web direction was improved compared to the original design. These results demonstrate the importance of considering time-dependent models when designing and optimizing slot coating processes, especially those involving structured fluids, which usually present thixotropic behavior.

The rheological thixotropy model considered in this work represents the behavior of a laponite suspension, but arbitrarily setting the avalanche and construction time to be the same.

As future work, it would be valuable to perform a complete rheological characterization of different slurries used in battery coating in order to perform die design analysis specific for this class of fluids. An optimized die design leads

to more uniform coated films and consequently improved performance of the coated electrodes.

7
Bibliography

ARIS, R. **Vectors, tensors and the basic equations of fluid mechanics**. [S.l.]: Courier Corporation, 2012.

BARNES, H. A. Thixotropy a review. **Journal of Non-Newtonian Fluid Mechanics**, v. 70, p. 1–33, 1997.

BROOKS, A. N.; HUGHES, T. J. Streamline upwind/petrov-galerkin formulations for convection dominated flows with particular emphasis on the incompressible navier-stokes equations. **Computer methods in applied mechanics and engineering**, Elsevier, v. 32, n. 1-3, p. 199–259, 1982.

CHIN, W. C. **Managed pressure drilling: modeling, strategy and planning**. [S.l.]: Gulf Professional Publishing, 2012.

FREDRICKSON, A. A model for the thixotropy of suspensions. **AIChe journal**, Wiley Online Library, v. 16, n. 3, p. 436–441, 1970.

GEUZAINE, C.; REMACLE, J.-F. Gmsh: A 3-d finite element mesh generator with built-in pre-and post-processing facilities. **International journal for numerical methods in engineering**, Wiley Online Library, v. 79, n. 11, p. 1309–1331, 2009.

HAN, W.; WANG, X. Optimal geometry design of the coat-hanger die with uniform outlet velocity and minimal residence time. **Journal of applied polymer science**, Wiley Online Library, v. 123, n. 4, p. 2511–2516, 2012.

HUANG, Y.; GENTLE, C. R.; HULL, J. B. A comprehensive 3-d analysis of polymer melt flow in slit extrusion dies. **Advances in Polymer Technology: Journal of the Polymer Processing Institute**, Wiley Online Library, v. 23, n. 2, p. 111–124, 2004.

IGALI, D. et al. Fluid flow in the coat-hanger die: Validation of the fluid velocity at the die outlet. **Materials Today: Proceedings**, Elsevier, v. 33, p. 1963–1966, 2020.

JAN, M.; WAGNER, N. J. Thixotropy. **Advances in Colloid and Interface Science**, v. 147, p. 214–227, 2009. ISSN 00018686.

KISTLER, S.; SCRIVEN, L. Coating flows. In: **Computational analysis of polymer processing**. [S.l.]: Springer, 1983. p. 243–299.

KISTLER, S. F.; SCHWEIZER, P. M. Coating science and technology: An overview. **Liquid Film Coating: Scientific principles and their technological implications**, Springer, p. 3–15, 1997.

LARSON, R. G.; WEI, Y. A review of thixotropy and its rheological modeling. **Journal of Rheology**, Society of Rheology, v. 63, p. 477–501, 5 2019. ISSN 0148-6055.

LIN, Y.-Y. et al. Coating die design for suspensions. **Asia-Pacific Journal of Chemical Engineering**, Wiley Online Library, v. 8, n. 1, p. 115–129, 2013.

LIU, T.-J.; LIU, L.-D.; TSOU, J.-D. A unified lubrication approach for the design of a coat-hanger die. **Polymer Engineering & Science**, Wiley Online Library, v. 34, n. 7, p. 541–550, 1994.

LOGG, A.; MARDAL, K.-A.; WELLS, G. **Automated solution of differential equations by the finite element method: The FEniCS book**. [S.l.]: Springer Science & Business Media, 2012. v. 84.

LOGG, A.; WELLS, G. N. Dolfin: Automated finite element computing. **ACM Transactions on Mathematical Software**, v. 37, 4 2010. ISSN 00983500.

MATSUBARA, Y. Geometry design of a coat-hanger die with uniform flow rate and residence time across the die width. **Polymer Engineering & Science**, Wiley Online Library, v. 19, n. 3, p. 169–172, 1979.

MATSUBARA, Y. Residence time distribution of polymer melt in the t-die. **Polymer Engineering & Science**, Wiley Online Library, v. 20, n. 3, p. 212–214, 1980.

MATSUBARA, Y. Residence time distribution of polymer melts in the linearly tapered coat-hanger die. **Polymer Engineering & Science**, Wiley Online Library, v. 23, n. 1, p. 17–19, 1983.

MENDES, P. R. de S.; ABEDI, B.; THOMPSON, R. L. Constructing a thixotropy model from rheological experiments. **Journal of Non-Newtonian Fluid Mechanics**, Elsevier B.V., v. 261, p. 1–8, 11 2018. ISSN 03770257.

MENDES, P. R. de S.; THOMPSON, R. L. A critical overview of elasto-viscoplastic thixotropic modeling. **Journal of Non-Newtonian Fluid Mechanics**, v. 187-188, p. 8–15, 11 2012. ISSN 03770257.

MENDES, P. R. S.; DUTRA, E. S. Viscosity function for yield-stress liquids. **Applied Rheology**, Kerschensteiner Verlag GmbH, v. 14, p. 296–302, 2004. ISSN 14306395.

MENG, K.; WANG, X.; CHEN, Q. Fluid flow in coat-hanger die of melt blowing process: Comparison of numerical simulations and experimental measurements. **Textile Research Journal**, v. 81, p. 1686–1693, 2011. ISSN 00405175.

MEWIS, J. Thixotropy-a general review. **Journal of Non-Newtonian Fluid Mechanics**, Elsevier, v. 6, n. 1, p. 1–20, 1979.

PEREZ, E.; CARVALHO, M. Drying of thin films of polymer solutions coated over impermeable substrates. **Heat transfer engineering**, Taylor & Francis, v. 28, n. 6, p. 559–566, 2007.

PÉTERFI, T. Die abhebung der befruchtungsmembran bei seeigeleiern: Eine kolloidchemische analyse des befruchtungsvorganges. **Wilhelm Roux'Archiv für Entwicklungsmechanik der Organismen**, Springer, v. 112, p. 660–695, 1927.

SECOR, R. B. Analysis and design of internal coating die cavities. In: **Liquid Film Coating: Scientific principles and their technological implications**. [S.l.]: Springer, 1997. p. 369–398.

WANG, X.; CHEN, T.; HUANG, X. Simulation of the polymeric fluid flow in the feed distributor of melt blowing process. **Journal of Applied Polymer Science**, v. 101, p. 1570–1574, 8 2006. ISSN 00218995.

YU, Y.-W.; LIU, T.-J. A simple numerical approach for the optimal design of an extrusion die. **Journal of Polymer Research**, Springer, v. 5, p. 1–7, 1998.